Hyperspectral Image Restoration Using Adaptive Anisotropy Total Variation and Nuclear Norms

Ting Hu, Wei Li, *Senior Member, IEEE,* Na Liu, Ran Tao, *Senior Member, IEEE,*
Feng Zhang, *Member, IEEE,* Paul Scheunders, *Senior Member, IEEE*

***Abstract*—Random Gaussian noise and striping artifacts are common phenomena in hyperspectral images (HSI). In this paper, an effective restoration method is proposed to simultaneously remove Gaussian noise and stripes by merging a denoising and a destriping submodel. A denoising submodel performs a multi-band denoising, i.e. Gaussian noise removal, considering Gaussian noise variations between different bands, to restore the striped HSI from the corrupted image, in which the striped HSI is constrained by a weighted nuclear norm. For the destriping submodel, we propose an adaptive anisotropy total variation method to adaptively smoothen the striped HSI, and we apply, for the first time, the truncated nuclear norm to constrain the rank of the stripes to 1. After merging the above two submodels, an ultimate image restoration model is obtained for both denoising and destriping. To solve the obtained optimization problem, the alternating direction method of multipliers (ADMM) is carefully schemed to perform an alternative and mutually constrained execution of denoising and destriping. Experiments on both synthetic and real data demonstrate the effectiveness and superiority of the proposed approach.**

***Index Terms*—Hyperspectral image, denoising and destriping, weighted nuclear norm, truncated nuclear norm, adaptive anisotropy total variation.**

I. Introduction

HYPERSPECTRAL images (HSI) are widely applied in remote sensing applications, such as agriculture, forestry and environmental science, because of their high spectral resolution, which allows to uniquely characterize many materials by their spectral response. However, when acquired by pushbroom sensors, HSI are easily polluted by Gaussian noise and striping artifacts. This does not only degrade the visual quality of HSI, but also impacts the performance of high-level tasks [1], such as classification [2], recognition [3], and detection [4]. Gaussian noise is usually caused by high temperature and poor lighting, while along-track stripes are the result of response non-uniformity and calibration errors in pushbroom detectors [5].

Recently, many denoising and destriping algorithms have been reported. The existing image denoising schemes are generally grouped in two categories [6]: learning-based and optimization-based approaches. Learning-based approaches remove noise by a mapping learned from pairs of clean and contaminated images [7]–[9]. However, lack of proper clean/contaminated image pairs makes these approaches unsuitable for real HSI denoising. Optimization-based approaches merge proper regularization terms into the ill-posed denoising inverse problem. Specifically, the observed image is expressed as:

$$\mathbf{Y} = \mathbf{X} + \mathbf{G}, \tag{1}$$

where $\mathbf{Y}$, $\mathbf{X}$, $\mathbf{G} \in \mathbb{R}^{M\times N\times B}$ are the third-order tensors with M rows, N columns and B bands, denoting the observed, polluted image, the clean image, and Gaussian noise, respectively. By maximum a posteriori (MAP) estimation, the following denoising model is obtained:

$$\min_{\mathbf{X}} \left\{ \frac{1}{2}\|\mathbf{Y}-\mathbf{X}\|_F^2 + \lambda \mathcal{J}(\mathbf{X}) \right\}, \tag{2}$$

where $\frac{1}{2}||\mathbf{Y}-\mathbf{X}||_F^2$ is the data fidelity term, λ is a regularization parameter, and $\mathcal{J}(\mathbf{X})$ is a regularization term, posing a priori constraint on the clean image, such as nonlocal self-similarity [10], [11], smoothness [12], or sparsity constraints [13].

Destriping methods can be classified into three categories: statistical, filtering-based, and optimization-based methods. Statistical methods [14], [15] are generally applied to single-band image destriping. Because of some statistical assumptions of stripes, their practicability is limited [16]. Methods that perform destriping by filtering [17]–[19], assume spatial periodicity of the stripes, but are known to produce blurring and staircase effects [20]. In the past decade, optimization-based destriping methods have grown. A striped image can be modeled as,

$$\mathbf{Y} = \mathbf{X} + \mathbf{S}, \tag{3}$$

where $\mathbf{S} \in \mathbb{R}^{M\times N\times B}$ is the image containing only the stripes. Optimization-based destriping methods [21]–[23], similar as in Eq. (2) were investigated. The regularization terms $\mathcal{J}(\mathbf{X})$, applied in [21]–[23] were respectively the Huber-Markov variation, the unidirectional total variation (TV), and the anisotropic TV, all of which exploited the gradient smoothness of the clean image. In [24], an improved destriping model was proposed by co-constraining the inherent characteristics of images and stripes:

$$\min_{\mathbf{X},\,\mathbf{S}} \left\{ \frac{1}{2}||\mathbf{Y}-\mathbf{X}-\mathbf{S}||_F^2 + \lambda_1\mathcal{J}_1(\mathbf{X}) + \lambda_2\mathcal{J}_2(\mathbf{S}) \right\}, \tag{4}$$

where λ_1 and λ_2 are the regularization parameters. $\mathcal{J}_1(\mathbf{X})$ and $\mathcal{J}_2(\mathbf{S})$ represent the anisotropy TV constraint on the clean

T. Hu, F. Zhang, W. Li and R. Tao are with the Beijing Key Laboratory of Fractional Signals and Systems, School of Information and Electronics, Beijing Institute of Technology, Beijing 100081, China (Corresponding author: R. Tao; rantao@bit.edu.cn).

N. Liu is with the College of Information Science and Technology, Beijing University of Chemical Technology, Beijing 100081, China.

P. Scheunders is with the IMEC-Vision Lab, Department of Physics, University of Antwerp, Belgium.

This work was supposed in part by the National Natural Science Foundation of China under Grants Nos. 91638201, 61922013, 61421001 and U1833203.

image and the nuclear norm on the stripes image, respectively. To the best of our knowledge, the existing variation-based destriping methods globally minimize the variation of an HSI, so that the unstriped parts of the image suffer from loss in texture information.

Although many effective denoising or destriping algorithms have been published, they generally do not work well on images corrupted by Gaussian noise and stripes simultaneously. The number of studies on the removal of mixed noise is limited. One obvious way is to perform denoising and destriping consecutively, but removing the one may damage the inherent statistical characteristics of the other [25], [26].

For an HSI, polluted by Gaussian noise and stripes, the degradation model can be modified as:

$$\mathbf{Y} = \mathbf{X} + \mathbf{S} + \mathbf{G}. \tag{5}$$

In [27], an effective model for the mixed noise removal was proposed, based on an optimization problem, similar as in Eq. (4), where $\mathcal{J}_1(\mathbf{X})$ and $\mathcal{J}_2(\mathbf{S})$ expressed the low-rank regularization of the clean image and the control of the upper cardinality bound of the stripes image, respectively. Some methods applied two regularization terms to the clean image:

$$\min_{\mathbf{X},\,\mathbf{S}} \left\{ \frac{1}{2}\|\mathbf{Y}-\mathbf{X}-\mathbf{S}\|_F^2 + \lambda_{11}\mathcal{J}_{11}(\mathbf{X}) + \lambda_{12}\mathcal{J}_{12}(\mathbf{X}) + \lambda_2\mathcal{J}_2(\mathbf{S}) \right\}. \tag{6}$$

In [26], $\mathcal{J}_{11}(\mathbf{X})$ and $\mathcal{J}_{12}(\mathbf{X})$ were the smoothness and sparsity constraints on the clean image. However, learning the sparsity priors directly from the noisy images was time-consuming and highly affected by the noise [13]. An upgraded version of the method in [27] was proposed by [28], in which $\mathcal{J}_{11}(\mathbf{X})$, $\mathcal{J}_{12}(\mathbf{X})$ and $\mathcal{J}_2(\mathbf{S})$ were the band-by-band TV and the nuclear norm of the clean image, and an L_1 sparsity prior on the stripes image, respectively. On top of exploiting the low-rankness and smoothness of the clean image to form $\mathcal{J}_{11}(\mathbf{X})$ and $\mathcal{J}_{12}(\mathbf{X})$, respectively, and using the same $\mathcal{J}_2(\mathbf{S})$ as [28], Xiong *et al*. [29] performed a nuclear norm constraint on the coding matrices from the clean image to achieve a better removal of the mixed noise. Whether the prior for stripes is obtained by a low-rank regularization through the nuclear norm or a sparsity constraint by the L_1 norm, both require manual tuning of the regularization parameters, which is a time-consuming effort.

Chen *et al*. [30] proposed an outstanding image low-rank restoration technique, by modeling the noise with non-independent identically distributed mixtures of Gaussians. However, no specific effort was done to model stripes. In addition, in the case of dense stripes, there is a potential risk of remaining stripes with the methods from [27]–[30], because all three methods constrain the clean images by the low-rank property, which also exists in stripes.

In summary, the state-of-the-art image restoration techniques are revealed with three main drawbacks: a loss of textural information in unstriped image regions when performing global variation on the clean image, the requirement of manual tuning of the regularization parameters when using the nuclear or l_1 norms to constrain the stripes image, and the potential risk of residual stripes when applying the low-rank constraint to clean image.

In this paper, we want to overcome these drawbacks, by proposing a new restoration model that merges a denoising and a destriping submodel. Specifically, we will impose a low-rank constraint on the striped image to remove Gaussian noise. Obviously, both the HSI and stripes image are highly spectrally redundant, thus, so does the striped HSI. When a cubic patch is extracted from a striped HSI, and vectorized, as in [27], it becomes a low-rank matrix. Thus, a low-rank regularization can effectively express the along-spectrum redundancy of the striped HSI.

One low-rank matrix approximation method, the low-rank matrix decomposition, has been successfully applied for HSI restoration [27], [28], [30], [31], but it is basically a nonconvex optimization problem [32]. Another, newer approximation approach for low-rank matrix approximations is the well-known nuclear norm minimization (NNM) [33], [34], which received considerable attention because it is easy to solve and performs very well.

However, NNM minimizes all singular values equally, while the larger singular values usually contain more important information [32]. Hence, a more flexible weighted NNM, with the ability to better preserve the larger singular values, was proposed and applied for state-of-the-art denoising in grayscale images [32]. Subsequently, a multi-channel version, accounting for noise variation between different channels (MC-WNNM) was proposed for color images denoising [10]. Both [32] and [10] constrain the low-rank matrices, obtained by a non-local search for similar patches in the image, hereby exploiting the non-local self-similarity of the clean image.

For HSI restoration, the weighted nuclear norm has been applied to regularize the along-spectrum redundancy of the clean HSI [35]–[37], which is conducive to saving memory and time compared to constraining the non-local self-similarity of the HSI. Inspired by this, we adopt the weighted nuclear norm to constrain the high redundancy of the striped HSI. Then, a multi-band denoising submodel, in which Gaussian noise variations between different bands are considered, is established by imposing a low-rank constraint, based on a weighted nuclear norm, on the striped HSI.

Secondly, a new destriping submodel is proposed to restore the clean HSI from the striped image, preserving texture information in unstriped regions while ensuring smoothness in striped regions. For this, an adaptive anisotropic TV is proposed. Since theoretically, each stripe can be expressed as a linear combination of all other stripes, stripes have rank 1. For this, we propose to apply the truncated nuclear norm [38], that better controls the rank of a matrix, without having to manually tune a parameter. Both the adaptive anisotropic TV and the truncated nuclear norm regularization terms are combined.

Since the striped HSI is a shared component of the two submodels, a restoration model is naturally formed by adding up the denoising and destriping submodels. Different from [27]–[30], the proposed HSI restoration method performs the low-rank constraint on the striped rather than on the clean HSI, to avoid possible residual stripes. In addition, denoising and destriping can be executed alternately by solving the proposed restoration model with the alternating direction method of multipliers (ADMM).

Overall, the contributions of this work are:

1) Given the along-spectrum redundancy in both stripes and HSI, the weighted nuclear norm is applied to regularize the striped image. A multi-band denoising submodel, using this weighted nuclear norm regularization (MB-WNN) is established to restore the striped image from the noisy and striped one, where Gaussian noise variations between bands are considered. Obviously, MB-WNN is also suitable to recover an HSI, corrupted by Gaussian noise only.
2) In order to preserve the edge information of the unstriped regions while imposing smoothness in the striped regions, an adaptive anisotropy TV is designed to regularize the clean image. Moreover, for the first time, the truncated nuclear norm is introduced to regularize stripes, without any manual tuning parameters, hereby exploiting the rank 1 of stripes. Then, a new destriping submodel, combining the adaptive anisotropy TV and the truncated nuclear norm (AATN) is established.
3) By carefully designing the striped HSI as a bridge between the two submodels, they are naturally merged to establish an HSI restoration model based on the adaptive anisotropy TV and the two nuclear norms (AANNs). The proposed AANNs is skillfully solved under the ADMM framework to alternatingly perform denoising and destriping.

The paper is arranged as follows. In Sec. II, we explain the proposed denoising and destriping submodels, along with the merged restoration method and the model optimization. Experimental results and discussion are presented in Sec. III, while the summary is given in Sec. IV.

II. Proposed Image Restoration Method (AANNs)

The restoration of an HSI requires the removal of both Gaussian noise and stripes. However, the successive application of denoising and destriping may lead to bad results, since the removal of one may affect the statistics of the other. Thus, it is important to link both processes appropriately. When the process of HSI denoising only removes Gaussian noise, and perfectly restores the striped HSI, the destriping task is not affected by the denoising. Hence, the goal is to use the striped HSI as a linked bridge between the two tasks of denoising and destriping.

First, Eq. (5) is split into the following two image models:

$$\mathbf{Y} = \mathbf{Xs} + \mathbf{G}, \tag{7}$$

$$\mathbf{Xs} = \mathbf{X} + \mathbf{S}, \tag{8}$$

where $\mathbf{Xs}$ represents the striped HSI. Then, in the denoising submodel, $\mathbf{Xs}$ is restored from $\mathbf{Y}$, and in the destriping submodel, $\mathbf{X}$ is recovered from $\mathbf{Xs}$. As the shared component of the two submodels, $\mathbf{Xs}$ closely links the denoising and destriping tasks. The final HSI restoration model for both denoising and destriping is naturally formed by merging the two submodels. Under the ADMM framework, denoising and destriping are performed alternately, as shown in Fig. 1. Compared to the consecutive application of denoising and destriping, such alternate processing can help the trade-off between denoising and destriping to achieve better restoration performance.

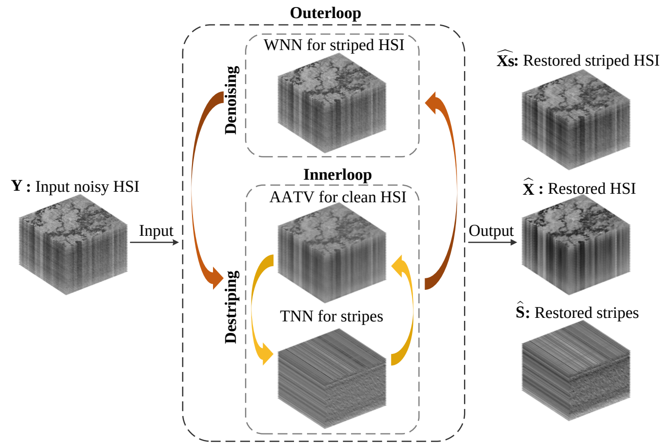

Fig. 1. Flowchart of the proposed AANNs for hyperspectral image restoration. WNN, AATV, and TNN correspond to the weighted nuclear norm, the adaptive anisotropy TV, and the truncated nuclear norm, respectively.

A. Denoising Submodel (MB-WNN)

A multi-band denoising submodel is developed to recover the striped HSI, that exploits the high redundancy of the striped HSI. Under the MAP theory, the estimation of $\mathbf{Xs}$ can be expressed as:

$$\hat{\mathbf{Xs}} = \arg\max_{\mathbf{Xs}} \Big\{ \ln p(\mathbf{Xs}|\mathbf{Y}) + \ln p(\mathbf{Xs}) \Big\}. \tag{9}$$

As it is known that the noise can vary between bands [10], [30], the different bands of the HSI are assumed to contain Gaussian noise that is with different standard deviations. Thus, the probability density $p(\mathbf{Xs}|\mathbf{Y})$ characterized by the statistics of the noise is given by:

$$p(\mathbf{Xs}|\mathbf{Y}) = H \exp\Big\{ -\frac{1}{2}||\mathbf{W}\cdot(\mathbf{Y}-\mathbf{Xs})||_F^2 \Big\}, \tag{10}$$

with:

$$H = \prod_{b=1}^{B} (2\pi\sigma_{nb}^2)^{-\frac{MNB}{2}}, \tag{11}$$

$$\mathbf{W}_b = \sigma_{nb}^{-1}\mathrm{I}, \ \mathrm{b} = 1, \cdots, \mathrm{B}, \tag{12}$$

where the symbol "$\cdot$" expresses the element-by-element multiplication, σ_{nb} is the standard deviation of Gaussian noise in band b of the HSI, $\mathbf{W}_b$ is band b of the weight tensor $\mathbf{W}$, and $\mathrm{I} \in \mathbb{R}^{\mathrm{M}\times\mathrm{N}}$, of which each element is 1.

Since there is no explicit expression for the probability of the unknown striped image, it is necessary to find a proper prior constraint to substitute $p(\mathbf{Xs})$. As described in Sec. I, the highly along-spectrum redundancy in both the HSI and stripes image can cause the striped HSI to be of low rank. Thus, we enforce a low-rank constraint on the striped HSI via the weighted nuclear norm. Specifically, a cubic patch of size

$h \times h \times B$ is first extracted from the striped HSI, and each band is stretched to a column vector. The weighted nuclear norm acts on the matrix formed by jointing these column vectors along the horizontal direction. To traverse the entire image, cubic patches are extracted at each step length $\text{floor}(h/2)$, from left to right and from top to bottom, where $\text{floor}(h/2)$ returns the integer, not higher than $(h/2)$.

We then have:

$$p(\mathbf{Xs}) \propto \exp(-\sum_{s=1}^{S} ||\mathcal{R}_s(\mathbf{Xs})||_{\omega,*}), \tag{13}$$

where S is the total number of the extracted cubic patches, $\mathcal{R}_s(\mathbf{Xs})$ represents the matrix formed by the s-th cubic patch, $||\mathcal{R}_s(\mathbf{Xs})||_{\omega,*} = \sum_i \omega_i \sigma_i[\mathcal{R}_s(\mathbf{Xs})]$ is the weighted nuclear norm of $\mathcal{R}_s(\mathbf{Xs})$, and $\sigma_i[\mathcal{R}_s(\mathbf{Xs})]$ are the singular values of $\mathcal{R}_s(\mathbf{Xs})$.

Plugging Eqs. (10) and (13) into Eq. (9), the following optimization problem is obtained:

$$\min_{\mathbf{Xs}} \Big\{ \frac{1}{2} ||\mathbf{W} \cdot (\mathbf{Y} - \mathbf{Xs})||_F^2 + \sum_{s=1}^{S} ||\mathcal{R}_s(\mathbf{Xs})||_{\omega,*} \Big\}, \tag{14}$$

where $\frac{1}{2}||\mathbf{W} \cdot (\mathbf{Y} - \mathbf{Xs})||_F^2$ is the multi-band weighted data fidelity term, and $\sum_{s=1}^{S} ||\mathcal{R}_s(\mathbf{Xs})||_{\omega,*}$ is the weighted nuclear norm regularization term. In [32], it is shown that the solution of this problem is obtained by soft thresholding of the singular values: $\max(\sigma_i[\mathcal{R}_s(\mathbf{Xs})] - \omega_i, 0)$. The weights are chosen as: $\omega_i = c/(\sigma_i[\mathcal{R}_s(\mathbf{Xs})] + \epsilon)$ with $\epsilon = 10^{-16}$ to avoid dividing by zero, and $c > 0$ is a constant. Because ω_i are inversely proportional to σ_i, the weighted nuclear norm constraints the larger singular values more weakly, and the smaller ones more strongly.

Although this method MB-WNN is established to recover the striped HSI, it is also suitable for HSI denoising. To demonstrate the method, a noisy image (Fig. 2(b)) is simulated by adding Gaussian noise of standard variation 0.05 to a clean image (Fig. 2(a)). In addition, a striped image (Fig. 3(a)) is produced by adding stripes of intensity 0.2 and density 0.2 to the clean image, and a noisy striped image (Fig. 3(b)) is generated by adding Gaussian noise of standard variation 0.025 to the striped image. As the denoising results show, the proposed MB-WNN outperforms MC-WNNM. The restored results have a clean appearance and look more similar to the original image (Fig. 2(d) versus 2(c) and Fig. 3(d) versus 3(c)). The running time of MC-WNNM and MB-WNN are 7340.67s and 108.62s, respectively, so MB-WNN is far more time efficient than MC-WNNM.

B. Destriping Submodel (AATN)

In order to remedy the loss of texture information in unstriped regions, caused by the global TV methods [21]–[24], [28], [29], and avoid the manual tuning parameter when constraining stripes [24], [26]–[29], a new destriping submodel is proposed.

Here, an adaptive anisotropy TV is proposed to adaptively perform TV regularization, limited to striped regions, so that

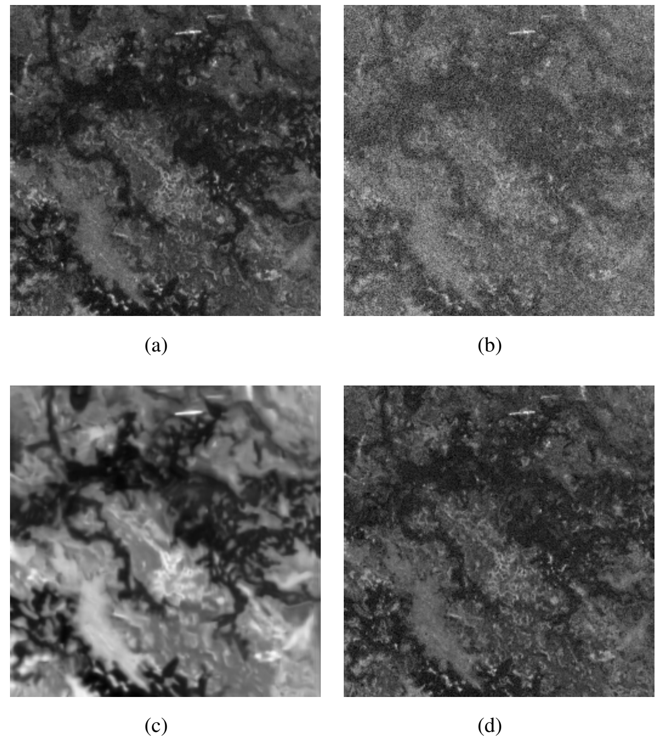

Fig. 2. (a) Original image. (b) Image corrupted by Gaussian noise. Restored images by (c) MC-WNNM and (d) the proposed MB-WNN.

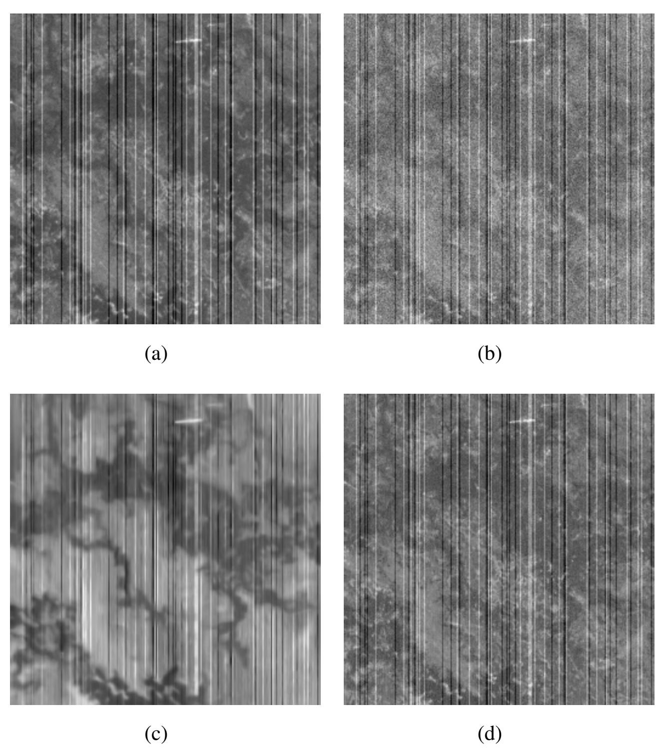

Fig. 3. (a) Striped image. (b) Noisy striped image. Restored striped image by (c) MC-WNNM and (d) the proposed MB-WNN.

texture information is preserved in unstriped regions. The key idea to design the adaptive anisotropy TV is that its regularization parameters are controlled by the gradients of the stripes, in such a way that no TV constraint is applied to regions without stripe gradients. Since along-track (vertical) stripes have no vertical gradient [23], the adaptive variation regularization is only applied in the spectral and horizontal directions. Theoretically, stripes are linearly dependent on each other, such that the rank of the stripes image should be 1. Hence, the truncated nuclear norm, a mathematical tool to accurately constrain the rank of a matrix [38], is utilized to constrain the rank of the stripes image to 1. Such truncated nuclear norm regularization for stripes avoids a manual tuning parameter. Combining the adaptive anisotropy TV and the truncated nuclear norm regularization, the following optimization problem is obtained:

$$\min_{\mathbf{X},\mathbf{S}} \left\{ \frac{1}{2}||\mathbf{Xs}-\mathbf{X}-\mathbf{S}||_F^2 + ||\mathbf{X}||_{AATV} + \sum_{b=1}^{B} ||\mathbf{S}_b||_r \right\}, \quad (15)$$

with

$$||\mathbf{X}||_{AATV} = ||\mathbf{\Lambda}_1 \cdot \bigtriangledown_x \mathbf{X}||_1 + ||\mathbf{\Lambda}_2 \cdot \bigtriangledown_z \mathbf{X}||_1, \quad (16)$$

$$\begin{cases} \mathbf{\Lambda}_1 = \min(|\bigtriangledown_x \mathbf{S}|, \mu_x) \\ \mathbf{\Lambda}_2 = \min(|\bigtriangledown_z \mathbf{S}|, \mu_z) \end{cases}, \quad (17)$$

$$\begin{cases} \bigtriangledown_x \mathbf{X} = \mathrm{D_x} * \mathbf{X} \\ \bigtriangledown_z \mathbf{X} = \mathrm{D_z} * \mathbf{X} \end{cases}, \quad \begin{cases} \bigtriangledown_x \mathbf{S} = \mathrm{D_x} * \mathbf{S} \\ \bigtriangledown_z \mathbf{S} = \mathrm{D_z} * \mathbf{S} \end{cases}, \quad (18)$$

where $||\mathbf{X}||_{AATV}$ expresses the adaptive anisotropy TV constraint on the clean image, $\mathbf{\Lambda}_1$ and $\mathbf{\Lambda}_2$ are the regularization parameter tensors, controlled by the spatial horizontal and spectral gradients of stripes to adaptively control the TV minimization; the symbols $\bigtriangledown_x$ and $\bigtriangledown_z$ represent the gradient operators along the horizontal and spectral directions, respectively; the minimum threshold function $\min(\theta, \phi)$, returning the smallest value of θ and ϕ avoids possible oversmoothing, caused by overlarge regularization parameters, μ_x and μ_z are the thresholds to limit the TV regularization along the horizontal and spectral directions, respectively; $*$ denotes the circular convolution operation, $\mathrm{D_x} = [1, -1]$ is the mask to obtain the horizontal gradient, and $\mathrm{D_z} = [1, -1]$ is the mask to obtain the along-spectrum gradient, $||\mathbf{S}_b||_r = \sum_{n=r}^{K} \sigma_n(\mathbf{S}_b)$ is the truncated nuclear norm of $\mathbf{S}_b$, $\mathbf{S}_b$ is band b of the stripes image, K is the number of nonzero singular values of $\mathbf{S}_b$, and r is set to 2, for constraining the rank of the stripes image to 1.

Fig.4 illustrates the proposed approach. A striped HSI (Fig. 4(b)) that is synthesized in the same way as Fig. 3(a) is processed by the proposed AATN, and the obtained results are presented in Figs. 4(c) and 4(e), revealing a successful separation of the image and stripes. Figs. 4(d) and 4(f) show the horizontal gradients of the true and estimated stripes images, respectively. The region denoted in orange is an unstriped region, and is lesser regularized by the adaptive anisotropy TV than the striped regions. This benefits the preservation of the textural information in the unstriped image regions.

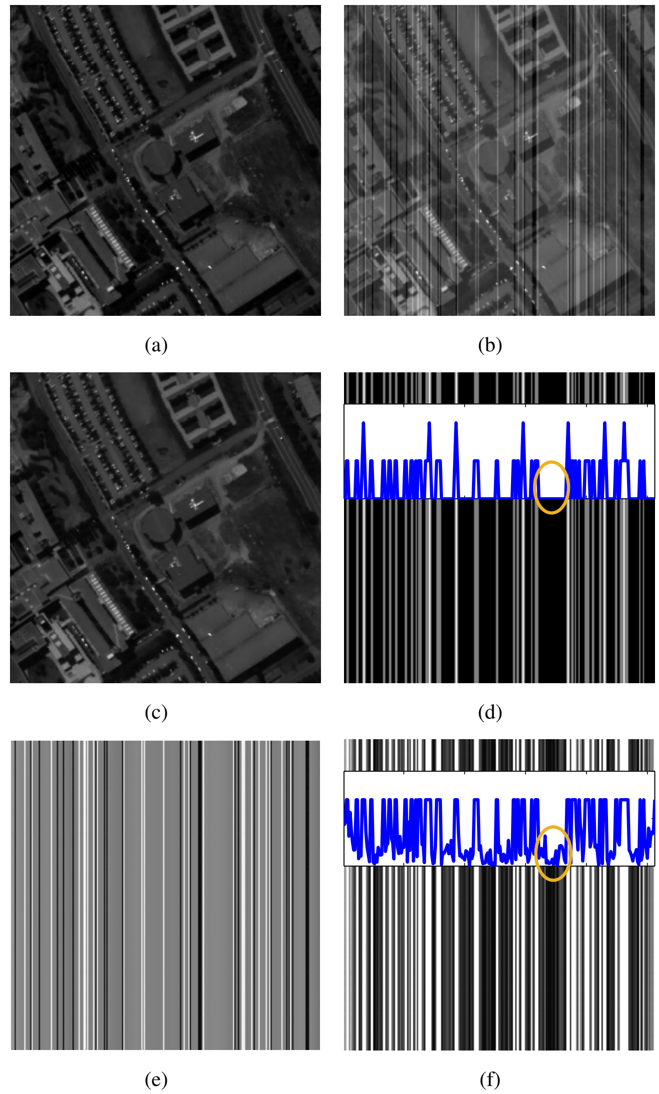

Fig. 4. Illustration of AATN. (a) Original image $\mathbf{X}$. (b) Striped image $\mathbf{Xs}$. (c) Estimated destriped image $\hat{\mathbf{X}}$. (d) Horizontal gradient of true stripes image $|\bigtriangledown_x \mathbf{S}|$. (e) Estimated stripes image $\hat{\mathbf{S}}$. (f) Horizontal gradient of estimated stripes image $\hat{\mathbf{\Lambda}}_1$. The pop outs in (d) and (f) plot row 200.

C. Total Restoration Model (AANNs)

Since the striped HSI $\mathbf{Xs}$ appears in Eq. (14) as well as in Eq. (15), the above two submodels can be directly added up to form the following optimization problem:

$$\begin{aligned} \min_{\mathbf{Xs},\mathbf{X},\mathbf{S}} \Big\{ & \frac{1}{2}||\mathbf{W}\cdot(\mathbf{Y}-\mathbf{Xs})||_F^2 + \sum_{s=1}^{S} ||\mathcal{R}_s(\mathbf{Xs})||_{\omega,*} \\ & + \frac{1}{2}||\mathbf{Xs}-\mathbf{X}-\mathbf{S}||_F^2 + ||\mathbf{X}||_{AATV} + \sum_{b=1}^{B} ||\mathbf{S}_b||_r \Big\}. \end{aligned} \quad (19)$$

Different from the state of the art restoration models, this model contains two data fidelity terms, namely, $\frac{1}{2}||\mathbf{W}\cdot(\mathbf{Y}-\mathbf{Xs})||_F^2$ and $\frac{1}{2}||\mathbf{Xs}-\mathbf{X}-\mathbf{S}||_F^2$, which helps to preserve more image information. Obviously, the estimation of $\mathbf{Xs}$ performs denoising, and the restoration of $\mathbf{X}$ performs destriping. As presented in Fig. 1, under the ADMM framework, the denoising and destriping processes are executed alternately rather than successively. Besides the ability of simultaneously eliminating Gaussian and striping noise, AANNs is easily reduced to two single-function models: MB-WNN for denoising and AATN for destriping.

Similar to Fig. 3(b), a noisy and striped HSI $\mathbf{Y}$ is produced. After processing the synthesized image $\mathbf{Y}$ with the proposed AANNs, the obtained estimations $\hat{\mathbf{X}}$ and $\hat{\mathbf{Xs}}$ are shown in Figs. 5(c) and 5(d), respectively. Fig. 5(d) shows that the proposed AANNs successfully performs both denoising and destriping.

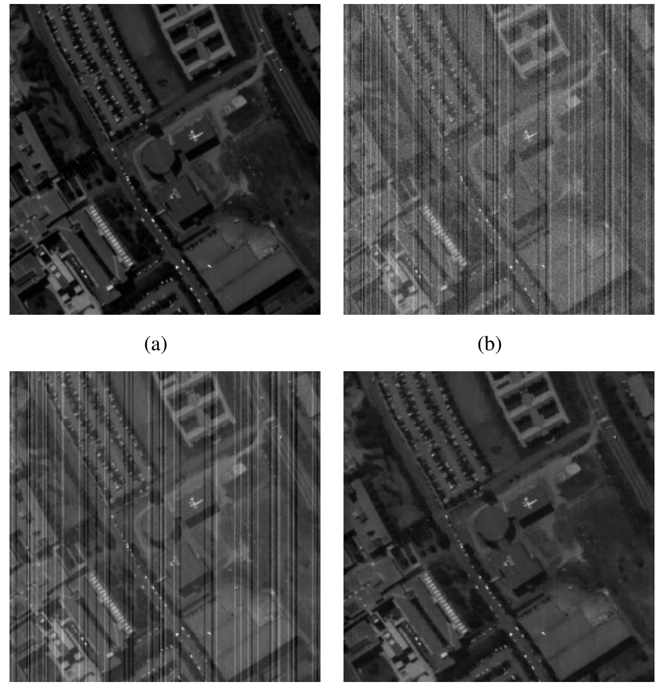

(a) (b) (c) (d)

Fig. 5. Illustration of the proposed restoration method. (a) Original image $\mathbf{X}$. (b) Noisy and striped image $\mathbf{Y}$. (c) Estimated striped image $\hat{\mathbf{Xs}}$. (d) Estimated image $\hat{\mathbf{X}}$.

D. Model Optimization

There is no analytical solution for AATV-NNs, but it can be split up into several, simple subproblems with closed-form solutions under the ADMM framework that is a well-known optimization framework with convergence guarantees. First, by introducing three auxiliary variables $\mathbf{T}$, $\mathbf{R}_1$, and $\mathbf{R}_2$, the proposed restoration model (19) is rewritten as:

$$\begin{aligned}&\min_{\mathbf{Xs},\mathbf{X},\mathbf{S},\mathbf{T},\mathbf{R}_1,\mathbf{R}_2}\Big\{\frac{1}{2}||\mathbf{W}\cdot(\mathbf{Y}-\mathbf{Xs})||_F^2+\sum_{s=1}^{S}||\mathcal{R}_s(\mathbf{T})||_{\omega,*}\\&+\frac{1}{2}||\mathbf{Xs}-\mathbf{X}-\mathbf{S}||_F^2+||\mathbf{\Lambda}_1\cdot\mathbf{R}_1||_1+||\mathbf{\Lambda}_2\cdot\mathbf{R}_2||_1+\\&\sum_{b=1}^{B}||\mathbf{S}_b||_r\Big\}\quad s.t.\ \mathbf{T}=\mathbf{Xs},\mathbf{R}_1=\triangledown_x\mathbf{X},\ \mathbf{R}_2=\triangledown_z\mathbf{X}.\end{aligned}\tag{20}$$

The augmented Lagrangian form of Eq. (20) is given by:

$$\begin{aligned}&\mathcal{L}(\mathbf{Xs},\mathbf{X},\mathbf{S},\mathbf{T},\mathbf{R}_j,\mathbf{A},\mathbf{C}_j)=\frac{1}{2}||\mathbf{W}\cdot(\mathbf{Y}-\mathbf{Xs})||_F^2\\&+\sum_{s=1}^{S}||\mathcal{R}_s(\mathbf{T})||_{\omega,*}+\frac{1}{2}||\mathbf{Xs}-\mathbf{X}-\mathbf{S}||_F^2\\&+||\mathbf{\Lambda}_1\cdot\mathbf{R}_1||_1+||\mathbf{\Lambda}_2\cdot\mathbf{R}_2||_1+\sum_{b=1}^{B}||\mathbf{S}_b||_r\\&+\langle\mathbf{A},\mathbf{T}-\mathbf{Xs}\rangle_F+\frac{\alpha}{2}||\mathbf{T}-\mathbf{Xs}||_F^2\\&+\langle\mathbf{C}_1,\mathbf{R}_1-\triangledown_x\mathbf{X}\rangle_F+\frac{\beta}{2}||\mathbf{R}_1-\triangledown_x\mathbf{X}||_F^2\\&+\langle\mathbf{C}_2,\mathbf{R}_2-\triangledown_z\mathbf{X}\rangle_F+\frac{\beta}{2}||\mathbf{R}_2-\triangledown_z\mathbf{X}||_F^2,\end{aligned}\tag{21}$$

where $j=1,2$, $\mathbf{A}$ and $\mathbf{C}_j$ are the augmented Lagrangian multipliers, and $\alpha>0$ and $\beta>0$ are the Lagrangian parameters. Next, the solution for each variable at iteration k is denoted by adding superscript k in the upper right corner of the variable symbol; for example, $\mathbf{X}^k$ is the solution of $\mathbf{X}$ at k-th iteration. Before solving the AANNs model, $\mathbf{Xs}^0$, $\mathbf{X}^0$, and $\mathbf{T}^0$ are initialized to $\mathbf{Y}$, while $\mathbf{S}^0$, $\mathbf{R}_j^0$, $\mathbf{A}^0$ and $\mathbf{C}_j^0$ are initialized to zero. Let the partial derivatives of $\mathcal{L}$ with respect to each function variable be zero, it follows that Eq. (19) is solved through alternately solving the following subproblems.

*1) **Xs** subproblem:* While fixing the other evaluated variables, $\mathbf{Xs}$ is obtained by solving:

$$\begin{aligned}\mathbf{Xs}^{k+1}=\arg\min_{\mathbf{Xs}}&\Big\{\frac{1}{2}||\mathbf{W}\cdot(\mathbf{Y}-\mathbf{Xs})||_F^2+\\&\frac{1}{2}\Big\|\mathbf{Xs}-\mathbf{X}^k-\mathbf{S}^k\Big\|_F^2+\frac{\alpha}{2}\Big\|\mathbf{T}^k-\mathbf{Xs}+\frac{\mathbf{A}^k}{\alpha}\Big\|_F^2\Big\}.\end{aligned}\tag{22}$$

This is a standard least squares optimization problem, with a closed-form solution [10]:

$$\begin{aligned}\mathbf{Xs}^{k+1}=&\left[\mathbf{W}\cdot\mathbf{W}\cdot\mathbf{Y}+\mathbf{X}^k+\mathbf{S}^k+\alpha\left(\mathbf{T}^k+\frac{\mathbf{A}^k}{\alpha}\right)\right]\\&\Big/(\mathbf{W}\cdot\mathbf{W}+\alpha+1),\end{aligned}\tag{23}$$

where the symbol "/" expresses the element-by-element division.

*2) **T** subproblem:* Let the partial derivative of $\mathcal{L}$ with respect to $\mathbf{T}$ be zero and the other variables be fixed. Then, the $\mathbf{T}$ subproblem is obtained:

$$\begin{aligned}\mathbf{T}^{k+1}=\arg\min_{\mathbf{T}}&\Big\{\frac{\alpha}{2}\Big\|\mathbf{T}-\mathbf{Xs}^k+\frac{\mathbf{A}^k}{\alpha}\Big\|_F^2\\&+\sum_{s=1}^{S}||\mathcal{R}_s(\mathbf{T})||_{\omega,*}\Big\}.\end{aligned}\tag{24}$$

Following Theorem 1 in [32]:

$$\mathcal{R}_s\Big(\mathbf{T}^{k+1}\Big)=\mathrm{U}\hat{\Sigma}\mathrm{V}^{\mathrm{T}},\tag{25}$$

where $\mathcal{R}_s\left(\mathbf{Xs}^k - \frac{\mathbf{\Lambda}^k}{\alpha}\right) = \mathrm{U}\Sigma\mathrm{V}^{\mathrm{T}}$, V^{T} denotes the transpose of V, and $\hat{\Sigma}$ is the solution of the following convex problem [10]:

$$\begin{aligned} &\min_{\hat{\sigma}_i}\left\{\sum_{i=1}^{L}\left[(\hat{\sigma}_i-\sigma_i)^2+\frac{2\omega_i}{\alpha}\hat{\sigma}_i\right]\right\} \\ &s.t.\ \ \hat{\sigma}_1 \geq \hat{\sigma}_2 \geq \cdots \geq \hat{\sigma}_L \geq 0, \end{aligned} \tag{26}$$

where σ_i and $\hat{\sigma}_i$ are the i-th diagonal elements of Σ and $\hat{\Sigma}$, respectively, and L denotes the number of non-zero singular values. According to [10], the solution of Eq. (26) is:

$$\hat{\sigma}_i = \begin{cases} 0, & c_2 < 0 \\ \frac{c_1+\sqrt{c_2}}{2}, & c_2 \geq 0 \end{cases} \tag{27}$$

where $c_1 = \sigma_i - \epsilon$, $c_2 = (\sigma_i - \epsilon)^2 - \frac{8c}{\alpha}$, and c is empirically set to $\sqrt{2B}$ [10], [32]. $\mathbf{T}^{k+1}$ is then generated by aggregating the S estimated matrices $\mathcal{R}_s\left(\mathbf{T}^{k+1}\right)$.

*3) **X** subproblem:* The $\mathbf{X}$ subproblem, extracted from the augmented Lagrangian function $\mathcal{L}$ is a least squares problem:

$$\begin{aligned} \mathbf{X}^{k+1} = \arg\min_{\mathbf{X}} &\left\{\frac{1}{2}\left\|\mathbf{Xs}^k - \mathbf{X} - \mathbf{S}^k\right\|_F^2 + \right. \\ \frac{\beta}{2}\left\|\mathbf{R}_1^k - \nabla_x\mathbf{X} + \frac{\mathbf{C}_1^k}{\beta}\right\|_F^2 &\left. + \frac{\beta}{2}\left\|\mathbf{R}_2^k - \nabla_z\mathbf{X} + \frac{\mathbf{C}_2^k}{\beta}\right\|_F^2\right\}, \end{aligned} \tag{28}$$

which can be solved by the fast Fourier transform (FFT) [23]:

$$\mathbf{X}^{k+1} = \mathcal{F}^{-1}\left(\mathbf{P}^k \big/ \mathbf{Q}^k\right), \tag{29}$$

with

$$\begin{cases} \mathbf{P}^k = \mathcal{F}\left(\mathbf{Xs}^k - \mathbf{S}^k\right) + \beta\left[\mathcal{F}^*(\mathrm{D_x})\cdot\mathcal{F}\left(\mathbf{R}_1^{\mathrm{k}} + \frac{\mathbf{C}_1^{\mathrm{k}}}{\alpha}\right)\right. \\ \left. +\mathcal{F}^*(\mathrm{D_z})\cdot\mathcal{F}\left(\mathbf{R}_2^{\mathrm{k}} + \frac{\mathbf{C}_2^{\mathrm{k}}}{\alpha}\right)\right] \\ \mathbf{Q}^k = 1 + \beta[\mathcal{F}(\mathrm{D_x})\cdot\mathcal{F}^*(\mathrm{D_x}) + \mathcal{F}(\mathrm{D_z})\cdot\mathcal{F}^*(\mathrm{D_z})] \end{cases}, \tag{30}$$

where $\mathcal{F}$ denotes the FFT, $\mathcal{F}^{-1}$ denotes the inverse FFT, and $\mathcal{F}^*$ performs the conjugate operation after FFT.

*4) **S** subproblem:* The stripes component $\mathbf{S}$ is updated by solving:

$$\mathbf{S}^{k+1} = \arg\min_{\mathbf{S}}\left\{\frac{1}{2}\left\|\mathbf{Xs}^k - \mathbf{X}^k - \mathbf{S}\right\|_F^2 + \sum_{b=1}^{B}||\mathbf{S}_b||_r\right\}. \tag{31}$$

Let $\mathbf{Ts} = \mathbf{Xs}^k - \mathbf{X}^k$. Then, SVD is performed on each band of $\mathbf{Ts}$, i.e., $\mathbf{Ts}_b = \mathrm{Us}\Sigma\mathrm{sVs}^{\mathrm{T}}$. According to Theorem 3.1 in [38], $\mathbf{S}_b$ is updated by

$$\mathbf{S}_b^{k+1} = \mathrm{Us}\hat{\Sigma}\mathrm{sVs}^{\mathrm{T}} \tag{32}$$

with

$$\hat{\sigma}_{si} = \begin{cases} \sigma_{si}, & 1 \leq i < r \\ 0, & r \leq i \leq K \end{cases}, \tag{33}$$

where $\hat{\sigma}_{si}$ and σ_{si} denote the i-th singular values in $\hat{\Sigma}$s and Σs, respectively.

5) $\boldsymbol{R}_j$ subproblem: Based on the obtained $\mathbf{X}^k$, $\mathbf{S}^k$, and $\mathbf{C}_j^k$, the $\mathbf{R}_j$ subproblem is expressed as:

$$\begin{aligned} \mathbf{R}_1^{k+1} = \arg\min_{\mathbf{R}_1} &\left\{\frac{\beta}{2}\left\|\mathbf{R}_1 - \nabla_x\mathbf{X}^k + \frac{\mathbf{C}_1^k}{\beta}\right\|_F^2\right. \\ &\left. + \left\|\mathbf{\Lambda}_1^k\cdot\mathbf{R}_1\right\|_1\right\}, \end{aligned} \tag{34}$$

$$\begin{aligned} \mathbf{R}_2^{k+1} = \arg\min_{\mathbf{R}_2} &\left\{\frac{\beta}{2}\left\|\mathbf{R}_2 - \nabla_z\mathbf{X}^k + \frac{\mathbf{C}_2^k}{\beta}\right\|_F^2\right. \\ &\left. + \left\|\mathbf{\Lambda}_2^k\cdot\mathbf{R}_2\right\|_1\right\}, \end{aligned} \tag{35}$$

where $\mathbf{\Lambda}_1^k$ and $\mathbf{\Lambda}_2^k$ are calculated by plugging $\mathbf{S}^k$ into Eq. (15). The solution of Eq. (34) is obtained by the soft-threshold operator [39]:

$$\mathbf{R}_1^{k+1} = \mathrm{Soft}\left(\nabla_{\mathrm{x}}\mathbf{X}^{\mathrm{k}} - \frac{\mathbf{C}_1^{\mathrm{k}}}{\beta}, \frac{\mathbf{\Lambda}_1^{\mathrm{k}}}{\beta}\right) \tag{36}$$

where $\mathrm{Soft}(\theta, \phi) = \mathrm{sign}(\theta)\cdot\max(|\theta| - \phi, 0)$. Similarly:

$$\mathbf{R}_2^{k+1} = \mathrm{Soft}\left(\nabla_{\mathrm{z}}\mathbf{X}^{\mathrm{k}} - \frac{\mathbf{C}_2^{\mathrm{k}}}{\beta}, \frac{\mathbf{\Lambda}_2^{\mathrm{k}}}{\beta}\right) \tag{37}$$

6) Multipliers subproblem: The augmented Lagrangian multipliers $\mathbf{A}$ and $\mathbf{C}_j$ are easily updated by:

$$\begin{cases} \mathbf{A}^{k+1} = \mathbf{A}^k + \alpha\left(\mathbf{T}^{k+1} - \mathbf{Xs}^{k+1}\right) \\ \mathbf{C}_1^{k+1} = \mathbf{C}_1^k + \beta\left(\mathbf{R}_1^{k+1} - \nabla_x\mathbf{X}^{k+1}\right) \\ \mathbf{C}_2^{k+1} = \mathbf{C}_2^k + \beta\left(\mathbf{R}_2^{k+1} - \nabla_z\mathbf{X}^{k+1}\right) \end{cases} \tag{38}$$

The procedure to solve the proposed AANNs is summarized in Alg. 1. The outerloop is stoppped when the number of iterations exceeds the preset threshold. The innerloop is stopped when the convergence condition $\frac{||\mathbf{X}^{k+1}-\mathbf{X}^k||_F^2}{||\mathbf{X}^k||_F^2} \leq tol$ is satisfied, or when the number of iterations exceeds the preset threshold. From Alg. 1, it is easy to infer the procedures of solving the submodels MB-WNN and AATN.

III. Experiments and Discussion

To validate the proposed methodology, in this section, experiments on both synthetic and real data are performed. The advantages of the weighted nuclear norm for denoising have been revealed before in [10], [32]. Thus, we will focus on the evaluation of the performance of the proposed AATN destriping submodel and the complete AANNs restoration model.

We will compare the proposed approach with a number of state of the art destriping and restoration methods from the literatures:

- The wavelet Fourier adaptive filter (WFAF) [19]. WFAF is a classical band-by-band destriping method, that removes stripes by an adaptive filter in the Fourier domain to the subbands obtained by a 2-D wavelet transform.

Algorithm 1 HSI reconstruction with AANNs

Input: Noisy and striped HSI $\mathbf{Y}$, weighted matrix $\mathbf{W}$, t_1, t_2
Initialization $\mathbf{Xs}^0$, $\mathbf{X}^0$, $\mathbf{T}^0 = \mathbf{Y}$; $\mathbf{S}^0$, $\mathbf{A}^0$, $\mathbf{C}_1^0$, $\mathbf{C}_2^0 = \mathbf{0}$
for $k_1 = 1 : t_1$ **do**
  Update $\mathbf{Xs}^{k_1}$ with Eq. (23)
  Update $\mathbf{T}^{k_1}$ by solving
  $\min_{\mathbf{T}} \left\{ \frac{\alpha}{2} \left\| \mathbf{T} - \mathbf{Xs}^{k_1} + \frac{\mathbf{A}^{k_1-1}}{\alpha} \right\|_F^2 + \sum_{s=1}^{S} ||\mathcal{R}_s(\mathbf{T})||_{\omega,*} \right\}$
  Update $\mathbf{A}^{k_1}$ as $\mathbf{A}^{k_1} = \mathbf{A}^{k_1-1} + \alpha(\mathbf{T}^{k_1} - \mathbf{Xs}^{k_1})$
  for $k_2 = 1 : t_2$ **do**
    Update $\mathbf{X}^{k_2}$ as $\mathbf{X}^{k_2} = \mathbf{P}^{k_2-1}/\mathbf{Q}^{k_2-1}$
    Update $\mathbf{S}^{k_2}$ in a band-by-band way, specifically, $\mathbf{S}_b^{k_2} = \mathrm{Us}\hat{\Sigma}\mathrm{sVs}$
    Update $\mathbf{R}_1^{k_2}$ and $\mathbf{R}_1^{k_2}$ singly as
    $\mathbf{R}_1^{k_2} = \mathrm{Soft}\big(\bigtriangledown_{\mathrm{x}} \mathbf{X}^{\mathrm{k}_2-1} - \mathbf{C}_1^{\mathrm{k}_2-1}/\beta, |\mathbf{\Lambda}_1^{\mathrm{k}_2-1}|/\beta \big)$,
    $\mathbf{R}_2^{k_2} = \mathrm{Soft}\big(\bigtriangledown_{\mathrm{z}} \mathbf{X}^{\mathrm{k}_2-1} - \mathbf{C}_2^{\mathrm{k}_2-1}/\beta, |\mathbf{\Lambda}_2^{\mathrm{k}_2-1}|/\beta \big)$
    Update $\mathbf{C}_1^{k_2}$ and $\mathbf{C}_1^{k_2}$ individually as
    $\mathbf{C}_1^{k_2} = \mathbf{C}_1^{k_2-1} + \beta\big(\mathbf{R}_1^{k_2} - \bigtriangledown_x \mathbf{X}^{k_2}\big)$,
    $\mathbf{C}_2^{k_2} = \mathbf{C}_2^{k_2-1} + \beta\big(\mathbf{R}_2^{k_2} - \bigtriangledown_z \mathbf{X}^{k_2}\big)$
    if (The convergence condition is satisfied) **then**
      break
    end if
  end for
end for
return $\mathbf{Xs}^{k_1}$, $\mathbf{X}^{k_2}$, and $\mathbf{S}^{k_2}$ to $\hat{\mathbf{X}}\mathbf{s}$, $\hat{\mathbf{X}}$, and $\hat{\mathbf{S}}$ in turn
Output: Results $\hat{\mathbf{X}}\mathbf{s}$, $\hat{\mathbf{X}}$, and $\hat{\mathbf{S}}$

- Anisotropic spatial-spectral TV (ASSTV) [23]. ASSTV performs destriping by minimizing the spatial-spectral TV of images.
- Low-rank multi-spectral image decomposition (LRMID) [24]. LRMID eliminates stripes by incorporating the spatial-spectral TV of the clean HSI and the nuclear norm of the stripes image into an image decomposition framework.
- Low-rank matrix recovery (LRMR) [27]. LRMR removes mixed noise, by employing the rank constraint on the clean image and the cardinality constraint on the stripes image.
- Total variation-regularized low-rank (LRTV) [28]. LRTV removes mixed noise, by minimizing the spectral TV of the HSI and the sparsity of the stripes image, along with performing a low-rank matrix decomposition of the HSI.
- L_0 gradient regularized low-rank tensor factorization (LRTFL_0) [29]. LRTFL_0 removes mixed noise, by performing a low-rank block term decomposition and an L_0 gradient constraint on the clean image, a nuclear norm constraint on the coding matrices of the clean image, and L_1 sparse regularization on the stripes image.
- Low-rank matrix factorization, combined with a non-independent identically distributed mixtures of Gaussians noise (NMoG-LRMF) [30]. NMoG-LRMF removes mixed noise, by imposing a low-rank matrix factorization on the clean image and modeling noise as non-independent identically distributed mixtures of Gaussians.

In a first set of experiments, the destriping performance of the proposed AATN submodel on synthetic striped data (i.e. real hyperspectral images on which stripes are synthetically added) is compared to WFAF and the state-of-the-art destriping algorithms ASSTV and LRMID. Since the restoration methods LRMR, LRTV, LRTFL_0, and NMoG-LRMF have been claimed to be effective destriping methods, they are also applied in the comparison.

The second set of experiments performs restoration of synthetic noisy and striped images (i.e. real hyperspectral images on which Gaussian noise and stripes are synthetically added). To assess the effect of the simultaneous application of the denoising and destriping submodels, we compare the proposed model AANNs with the denoising submodel MB-WNN, the destriping submodel AATN, and the successive application of both submodels (i.e. the application of the destriping submodel AATN after the denoising submodel MB-WNN). We will refer to the latter as W-AATN. Moreover, we will compare the restoration performance to the state-of-the-art restoration techniques LRMR, LRTV, LRTFL_0, and NMoG-LRMF.

TABLE I
DETAILS OF THE COMPARED METHODS

Method	Applied mathematical techniques	Ability
WFAF	1. 2-D wavelet transform for each band; 2. Fourier filtering for wavelet subbands.	Destriping
ASSTV	1. Spatial-spectral TV for clean image.	Destriping
LRMID	1. Spatial-spectral TV for lean image; 2. Nuclear norm for stripes.	Destriping
LRMR	1. Rank constraint on clean image; 2. Cardinality constraint on stripes.	Destriping and denoising
LRTV	1. Spectral TV on clean image; 2. Low-rank constraint on clean image; 3. Sparsity constraint on stripes.	Destriping and denoising
LRTFL_0	1. Block term decomposition for clean ima--ge; 2. Nuclear norm for coding matrices; 3. L_0 gradient constraint on clean image; 4. Sparsity constraint on stripes.	Destriping and denoising
NoMG -LRMF	1. Low-rank matrix factorization for clean image; 2. Mixtures of Gaussian model for noise.	Destriping and denoising
MB-WNN	1. Weighted nuclear norm for restored ima--ge.	Denoising
AATN	1. Adaptive anisotropy TV for clean image; 2. Truncated nuclear norm for stripes.	Destriping
W-AATN	1. Weighted nuclear norm for striped image; 2. Adaptive anisotropy TV for clean image; 3. Truncated nuclear norm for stripes.	Denoising and then destriping
AANNs	1. Weighted nuclear norm for striped image; 2. Adaptive anisotropy TV for clean image; 3. Truncated nuclear norm for stripes.	Destriping and denoising

The final experiment processes a real, contaminated HSI, to evaluate the practical value of the proposed method when compared to the state-of-the-art methods. To clearly present the differences of the compared methods, they are summarized in Table I.

A. Experimental Setup

1) Experimental Data: To qualitatively and quantitatively evaluate the proposed methods, two hyperspectral datasets, are carefully selected to synthesize the striped and noisy images.

1. Botswana image [1], of size $1476 \times 256 \times 242$, was captured by the NASA EO-1 satellite over the Okavango Delta, Botswana. This data contains swamps and drier woodlands and is relatively smooth. After removing uncalibrated and water absorption bands ([10-55, 82-97, 102-119, 134-164, 187-220]), 145 bands are remaining. An arbitrary subimage of size $256 \times 256 \times 145$ is cropped from the Botswana image.

2. University of Pavia image, acquired by the ROSIS sensor over Pavia university in nothern Italy is of size 610×340 with 103 spectral bands. The first ten invalid bands are discarded. As an urban dataset, it provides abundant shape structure and texture information. A subimage of size $256 \times 256 \times 93$ was cropped for the experiments.

Both data sets are linearly normalized to $[0, 1]$, as in [27]. Just like in [23], [24], the striped data is synthesized in a band-by-band manner. Specifically, a value η is added to each pixel in $\mathrm{round}(\gamma \mathrm{N})/2$ columns, randomly selected from each image band. Similarly, a value $-\eta$ is added to another randomly selected $\mathrm{round}(\gamma \mathrm{N}/2)$ columns, where $\mathrm{round}(\phi)$ returns the integer result of the rounding of ϕ. η and γ denote the intensity and density of the stripes, respectively. In addition, on each band of the striped images, Gaussian noise with a specific standard deviation σ_n is added. The restored images are stretched to the original scale.

To validate the practical use of the proposed restoration approach, an image of size $499 \times 500 \times 75$, captured by the Tiangong-I spectroradiometer [2] [40] is used. The Tiangong-I image contains real noise arising from the actual imaging sensor. An image block of size $256 \times 256 \times 40$ is cut from the original image, in which 35 water absorption bands (i.e., 1-2, 13, 20-23, 31, 33, 36-43, 45, 48, 53, 61-75) are discarded.

2) Performance Metrics: To quantitatively assess the reconstruction performance, four quantitative metrics are calculated:

$$\mathrm{PSNR} = \frac{1}{B}\sum_{b=1}^{B} 10\log\frac{65535^2 \times MN}{\sum\limits_{i=1}^{M}\sum\limits_{j=1}^{N}\left[\hat{\mathbf{X}}_b(i,j) - \mathbf{X}_b(i,j)\right]}$$

$$\mathrm{SSIM} = \frac{1}{B}\sum_{b=1}^{B}\frac{(2\mu_{\hat{\mathbf{X}}_b}\mu_{\mathbf{X}_b} + C_1)(2\sigma_{\hat{\mathbf{X}}_b\mathbf{X}_b} + C_2)}{(\mu^2_{\hat{\mathbf{X}}_b} + \mu^2_{\mathbf{X}_b} + C_1)(\sigma_{\hat{\mathbf{X}}_b} + \sigma_{\mathbf{X}_b} + C_2)}$$

$$\mathrm{SAM} = \frac{1}{MN}\sum_{i=1}^{M}\sum_{j=1}^{N}\arccos\frac{\sum\limits_{b=1}^{B}\mathbf{X}_b(i,j)\hat{\mathbf{X}}_b(i,j)}{\sqrt{\sum\limits_{b=1}^{B}\mathbf{X}_b^2(i,j)\sum\limits_{b=1}^{B}\hat{\mathbf{X}}_b^2(i,j)}}$$

$$\mathrm{SID} = \frac{1}{MN}\sum_{i=1}^{M}\sum_{j=1}^{N}\left[\sum_{b=1}^{B}\mathbf{p}_b(i,j)\log\frac{\mathbf{p}_b(i,j)}{\mathbf{q}_b(i,j)} + \sum_{b=1}^{B}\mathbf{q}_b(i,j)\log\frac{\mathbf{q}_b(i,j)}{\mathbf{p}_b(i,j)}\right]$$

[1]http://www.ehu.eus/ccwintco/index.php?title=Hyperspectral_Remote_Sensing_Scenes

[2]http://en.cmse.gov.cn/

with

$$\begin{cases} \mathbf{p}_b(i,j) = \frac{\mathbf{X}_b(i,j)}{\sum\limits_{b=1}^{B}\mathbf{X}_b(i,j)} \\ \mathbf{q}_b(i,j) = \frac{\hat{\mathbf{X}}_b(i,j)}{\sum\limits_{b=1}^{B}\hat{\mathbf{X}}_b(i,j)} \end{cases}$$

where $\hat{\mathbf{X}}_b$ and $\mathbf{X}_b$ express band b of the clean and restored images, respectively, $\mu_{\hat{\mathbf{X}}_b}$ and $\mu_{\mathbf{X}_b}$ are the means of $\hat{\mathbf{X}}_b$ and $\mathbf{X}_b$, respectively, $\sigma_{\mathbf{X}_b}$ and $\sigma_{\hat{\mathbf{X}}_b}$ are the variances of $\hat{\mathbf{X}}_b$ and $\mathbf{X}_b$, respectively, $\sigma_{\hat{\mathbf{X}}_b\mathbf{X}_b}$ is the covariance between $\hat{\mathbf{X}}_b$ and $\mathbf{X}_b$, and C_1 and C_2 are constants to maintain stability.

The peak signal-to-noise ratio (PSNR) and structural similarity (SSIM) measure the spatial restoration performance. The higher the values of PSNR and SSIM, the better the reconstruction. The spectral angle mapper (SAM) and spectral information divergence (SID) evaluate the spectral fidelity. The lower SAM and SID, the lower the spectral distortion.

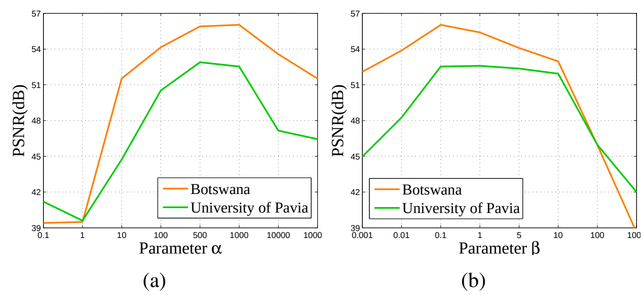

Fig. 6. Parameter tuning for AANNs using PSNR on two synthetic data sets ($\eta = 0.2$, $\gamma = 0.2$, and $\sigma_n = 0.05$)). (a) Tuning α when $\beta = 0.1$. (b) Tuning β when $\alpha = 1000$.

3) Parameter Settings: During all the experiments, the convergence threshold tol is set to 10^{-4}. α and β are empirically tuned by the experimental results (see the examples in Fig. 6 for more details), while μ_x and μ_z are tuned following [24]. Specifically, for AATN, the Lagrangian parameter β is set to 0.1, the maximum number of iteration t_2 is set to 50, and the threshold parameters are tuned depending on the degree of striping with tuning ranges $\mu_x \in [0.001, 0.03]$ and $\mu_z \in [0.001, 0.005]$, respectively. The parameters, involved in AANNs are set as follows: $t_1 = 5$, $t_2 = 6$, $h = 10$, $\alpha = 1000$, $\beta = 0.1$, μ_x and μ_z are tuned within the ranges above. For the compared algorithms, the parameters are tuned, following [19], [23], [24], [27]–[30]. For a real HSI that contains both Gaussian noise and stripes, the method [41] is carefully chosen to estimate the Gaussian noise level σ_{nb} of each band. The method [41] calculates the noise variance based on the relationship between the image eigenvalues and the noise level, and relies on the low-rank property of the clean image. The introduction of stripes causes little effect on this property. Thus, the existence of stripes hardly degrades the accuracy of the chosen estimation method.

Using the above parameter settings, PSNR and SAM are calculated during the iteration process to demonstrate the convergence of Alg. 1. As shown in Fig. 7, the PSNR and SAM of both data sets gradually converge to stable values.

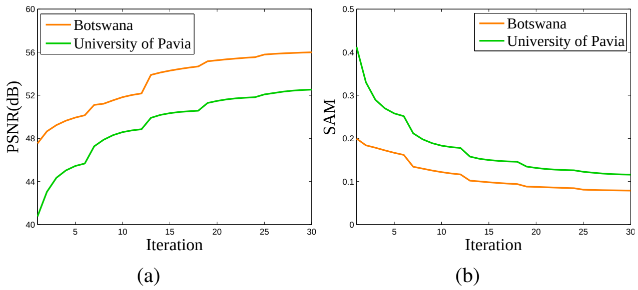

Fig. 7. PSNR and SAM in function of the number of iterations on two synthetic data sets ($\eta = 0.2$, $\gamma = 0.2$, and $\sigma_n = 0.05$) to demonstrate the convergence of Alg. 1. (a) PSNR and (b) SAM.

B. Experiments on Synthetically Corrupted HSI

1) Experiments on Striped data: The destriping performance metrics of the different methods for the restoration of images, corrupted by stripes of different intensities and densities are listed in Tables II and III. Since real HSI can be corrupted by dense stripes, the destriping results on images with dense stripes ($\eta = 0.4$, $\gamma = 0.6$) are shown in Figs. 8 and 9 for a visual evaluation of the destriping performance of the various algorithms.

When comparing the proposed destriping submodel AATN with the destriping methods WFAF, ASSTV, LRMID, one can conclude that WFAF shows the poorest results. ASSTV shows a better destriping performance, but is no match for LRMID, that entails a constraint on stripes. The proposed AATN outperforms the latter three methods. This demonstrates the effectiveness of the strategies of smoothing the striped regions while preserving the unstriped regions, along with the use of the truncated nuclear norm constraint on the stripes.

When comparing the proposed destriping submodel AATN with the restoration methods LRMR, LRTV, LRTFL_0, and NoMG-LRMF, the following can be concluded. LRMR shows the worst destriping performance. LRTFL_0 that imposes three constraints on the clean image and a single constraint on stripes, performs better than LRMR but worse than the proposed AATN (especially for serious striping). The worse destriping performance of LRTFL_0 could be the result of its imbalanced regularization between the clean image and stripes, possibly causing the over-loss of image information and the maintaining of stripes (see Figs. 8(h) and 9(h)). LRTV and NMoG-LRMF however outperform AATN on the Botswana data with sparser stripes (specifically, $\gamma = 0.2, 0.4$), whereas for the University of Pavia data, it is the other way around. In general, the destriping performance of LRMR, LRTV, and NMoG-LRMF seems to be highly dependent on the texture complexity of the images and on the spatial density of the stripes. As can be seen from the results (Tables II and III, Figs. 8(e)-8(i) and 9(e)-9(i)), their destriping performance seriously deteriorates with the density of stripes, and is much lower on the University of Pavia image than on the smoother Botswana image. Since these three methods have in common that they impose the low-rank constraint on the clean HSI, a possible cause is that dense stripes may possess stronger low-rank properties than the clean image. In case of complex textures, even sparse stripes may have stronger low-rank properties than the clean images. The destriping performance of AATN slowly declines with increasing stripe intensity and density, yet remains stable irrespective of the image smoothness. We can conclude that the proposed AATN is an effective destriping method and competitive to the state-of-the-art techniques, in particular for dense stripes and for highly textured images.

2) Experiments on Noisy and Striped Data: In this experiment, different levels of stripes and Gaussian noise are added to the Botswana and University of Pavia images, to validate the restoration capability of the proposed AANNs. Gaussian noise is added, either with standard deviations ($\sigma_n = 0.025, 0.05, 0.1$), equally on all bands, or with standard deviations that vary between bands, in the range ($\sigma_n \in (0, 0.1]$). Sparse ($\eta = 0.2$, $\gamma = 0.2$) as well as dense ($\eta = 0.4$, $\gamma = 0.6$) stripes are added. The proposed restoration method is compared to the denoising submodel (MB-WNN), the destriping submodel (AATN), the successive application of the denoising and destriping submodels (W-AATN) and the restoration methods LRMR, LRTV, LRTFL_0, and NMoG-LRMF. The corresponding results are presented in Tables IV-V and Figs. 10-11.

From the results, the following conclusions can be drawn:

- The application of both denoising and destriping (W-AATN and AANNs) outperforms the application of only the denoising submodel (MB-WNN) and the application of only the destriping submodel (AATN). In general, the proposed joint denoising and destriping strategy outperforms the successive application of the denoising and destriping submodels. This is due to the alternating iteration procedure, balancing the denoising and destriping processes in the proposed method AANNs, while the destriping process in the W-AATN method may be affected by the denoising step.
- Because of its imbalance in constraining the clean image and stripes, LRTFL_0 performs worse than the proposed AANNs in the removal of stripes. This can be observed in Fig. 10(e) versus Fig. 10(j). Similar as in the destriping experiment, the restoration performance of LRMR, LRTV, and NMoG-LRMF largely reduces with an increase in the image texture complexity and/or in the density of stripes, as a consequence of applying the low-rank constraint directly on the clean image. In addition, LRMR and LRTV perform poor on the destriping, as is clearly visible in Figs. 10(c)-10(d) and 11(c)-11(d).
- From the values of PSNR, SAM, and SID in Tables IV and V, NMoG-LRMF seems to outperform the proposed method. However, its SSIM values are always lower. SSIM describes the image distortion by comparing luminance (mean), contrast (standard deviation), and structure [42]. As can be observed, Fig. 10(f) is brighter than the original image Fig. 10(a), which explains that the lower values of SSIM is the result of loss of luminance and contrast information.
- The proposed AANNs imposes the low-rank constraint on the striped image rather than on the clean image, and applies the adaptive smoothness regularization on

TABLE II

PERFORMANCE METRICS ON THE BOTSWANA IMAGE FOR DIFFERENT LEVELS OF STRIPES

Metrics	Method	$\eta=0.2$				$\eta=0.4$				$\eta=0.6$				$\eta=0.8$			
		γ				γ				γ				γ			
		0.2	0.4	0.6	0.8	0.2	0.4	0.6	0.8	0.2	0.4	0.6	0.8	0.2	0.4	0.6	0.8
PSNR	Degraded	46.22	43.21	41.42	40.18	40.20	37.19	35.40	34.16	36.68	33.67	31.87	30.63	34.18	31.17	29.38	28.14
	WFAF	56.26	54.22	53.68	52.71	53.14	50.75	49.49	48.79	51.15	48.40	47.02	45.77	49.17	46.90	44.41	44.01
	ASSTV	56.46	55.62	54.51	54.10	54.16	53.16	52.11	51.11	52.13	50.97	49.97	48.54	50.37	49.09	47.64	47.08
	LRMID	57.70	56.47	55.79	54.56	55.92	54.38	53.35	53.08	53.56	52.53	51.80	50.68	52.49	51.41	50.64	49.27
	LRMR	54.60	52.90	51.61	50.85	50.82	48.73	47.23	46.29	48.15	45.52	44.16	42.83	47.07	43.81	41.69	40.52
	LRTV	62.45	58.84	55.07	51.43	62.01	58.40	52.16	49.05	61.86	58.17	51.74	47.40	61.25	57.76	50.94	47.39
	LRTFL_0	58.06	**59.68**	54.81	51.35	58.66	57.54	53.54	48.22	59.00	57.40	51.52	46.25	56.09	56.00	52.92	45.35
	NMoG-LRMF	**66.16**	58.87	54.70	54.50	**65.74**	**60.07**	**54.11**	**53.25**	**65.47**	**60.04**	**54.02**	**51.65**	**65.43**	**59.94**	**53.96**	**50.17**
	AATN	58.07	57.37	**56.13**	**55.52**	56.14	54.26	53.60	52.57	54.42	52.66	51.80	50.78	53.14	51.83	50.66	49.57
SSIM	Degraded	0.9606	0.9247	0.8901	0.8597	0.8713	0.7723	0.6882	0.6238	0.7720	0.6177	0.5097	0.4310	0.6821	0.4940	0.3761	0.297
	WFAF	0.9951	0.9930	0.9920	0.9901	0.9900	0.9833	0.9776	0.9743	0.9816	0.9714	0.9610	0.9492	0.9687	0.9527	0.9396	0.9265
	ASSTV	0.9928	0.9922	0.9904	0.9897	0.9884	0.9872	0.9844	0.9768	0.9819	0.9793	0.9738	0.9572	0.9709	0.9652	0.9461	0.9482
	LRMID	0.9964	0.9951	0.9924	0.9900	0.9937	0.9922	0.9881	0.9871	0.9902	0.9860	0.9841	0.9792	0.9862	0.9828	0.9800	0.9719
	LRMR	0.9929	0.9893	0.9859	0.9834	0.9832	0.9739	0.9632	0.9556	0.9700	0.9468	0.9289	0.9058	0.9631	0.9260	0.8798	0.8435
	LRTV	0.9984	0.9961	0.9911	0.9803	0.9986	0.9956	0.9826	0.9620	0.9985	0.9909	0.9798	0.9444	0.9986	0.9892	0.9763	0.9361
	LRTFL_0	0.9969	**0.9981**	0.9930	0.9718	0.9973	**0.9969**	0.9821	0.9328	0.9979	**0.9967**	0.9758	0.8924	0.9956	**0.9956**	0.9680	0.8698
	NMoG-LRMF	**0.9996**	0.9859	0.9876	0.9873	**0.9996**	0.9852	0.9773	0.9836	**0.9996**	0.9851	0.9740	0.9766	**0.9996**	0.9851	0.9732	0.9663
	AATN	0.9965	0.9953	**0.9931**	**0.9926**	0.9940	0.9918	**0.9901**	**0.9877**	0.9908	0.9870	**0.9848**	**0.9819**	0.9884	0.9844	**0.9808**	**0.9762**
SAM	Degraded	0.2310	0.3225	0.3883	0.4406	0.4333	0.5791	0.6737	0.7436	0.5996	0.7665	0.8678	0.9365	0.7321	0.9043	0.9997	1.0647
	WFAF	0.0625	0.0740	0.0849	**0.0902**	0.0904	0.1245	0.1401	0.1578	0.1390	0.1711	0.1941	0.2198	0.1615	0.2110	0.2443	0.2853
	ASSTV	0.0936	0.0984	0.1092	0.1154	0.1207	0.1382	0.1493	0.2630	0.1616	0.1772	0.2089	0.2781	0.2133	0.2484	0.3288	0.3050
	LRMID	0.0760	0.0908	0.1154	0.1333	0.1039	0.1248	0.1363	0.1435	0.1367	0.1451	0.1531	0.1755	0.1463	0.1617	0.1728	0.2084
	LRMR	0.0959	0.1181	0.1370	0.1491	0.1476	0.1864	0.2095	0.2366	0.1906	0.2594	0.3018	0.3529	0.2002	0.2919	0.4170	0.4978
	LRTV	0.0330	0.0502	0.0780	0.1250	0.0275	0.0546	0.1368	0.2168	0.0286	0.1187	0.1623	0.2787	0.0285	0.1291	0.1722	0.3249
	LRTFL_0	0.0568	**0.0461**	**0.0769**	0.1810	0.0552	**0.0527**	0.1463	0.2883	0.0476	**0.0526**	0.1458	0.4099	0.0674	**0.0616**	0.2361	0.4823
	NMoG-LRMF	**0.0247**	0.1382	0.1478	0.1479	**0.0216**	0.1387	0.1485	0.1480	**0.0254**	0.1390	0.1486	**0.1491**	**0.0251**	0.1436	**0.1495**	**0.1580**
	AATN	0.0665	0.0743	0.0881	0.0909	0.0820	0.1049	**0.1069**	**0.1234**	0.1024	0.1257	**0.1449**	0.1659	0.1213	0.1402	0.1611	0.1767
SID	Degraded	49.91	98.01	149.64	198.55	151.79	303.84	460.69	614.32	239.26	484.27	732.82	974.50	228.80	455.44	690.30	916.24
	WFAF	18.60	19.56	24.09	26.06	25.52	34.57	40.01	46.47	39.01	49.77	62.50	74.31	52.17	70.72	95.92	110.70
	ASSTV	19.63	21.03	25.43	25.05	26.89	28.79	33.79	43.35	35.03	41.36	52.42	75.65	50.60	63.03	97.65	93.90
	LRMID	10.89	12.99	22.02	27.79	20.13	22.58	32.36	32.37	25.62	35.14	39.82	47.52	35.38	40.90	46.56	59.75
	LRMR	16.92	21.95	28.27	32.42	32.06	43.69	55.69	65.33	48.11	76.41	104.84	145.14	53.51	100.60	193.83	269.25
	LRTV	**2.53**	**6.07**	17.01	33.18	**3.89**	**6.73**	33.39	67.25	4.99	15.69	41.33	100.34	6.74	16.37	46.14	110.58
	LRTFL_0	6.96	6.27	**11.98**	38.43	7.51	7.99	31.15	93.21	4.94	**10.32**	**37.18**	169.27	13.70	**15.33**	50.08	188.09
	NMoG-LRMF	3.16	28.70	25.24	26.02	4.04	32.50	42.64	**29.56**	**1.58**	36.97	49.68	51.65	**1.99**	39.44	52.64	54.69
	AATN	17.18	19.77	22.80	**24.91**	22.55	26.31	**29.03**	32.61	27.24	33.09	38.49	**43.65**	31.14	37.38	**43.80**	**50.98**

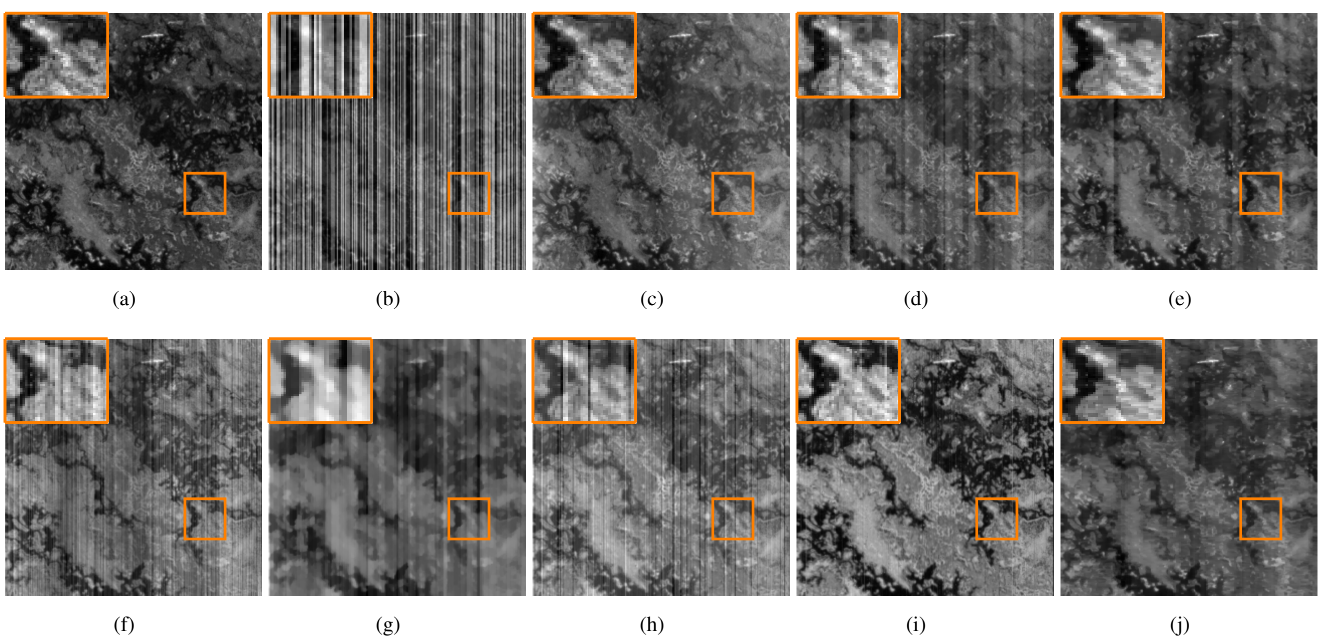

Fig. 8. Band 10 of the Botswana image. (a) Original clean image. (b) Striped image ($\eta = 0.4$ and $\gamma = 0.6$). Destriped images generated by (c) WFAF, (d) ASSTV, (e) LRMID, (f) LRMR, (g) LRTV, (h) LRTFL_0, (i) NMoG-LRMF, and (j) AATN.

TABLE III
PERFORMANCE METRICS ON THE UNIVERSITY OF PAVIA IMAGE FOR DIFFERENT LEVELS OF STRIPES

Metrics	Method	$\eta = 0.2$				$\eta = 0.4$				$\eta = 0.6$				$\eta = 0.8$			
		γ				γ				γ				γ			
		0.2	0.4	0.6	0.8	0.2	0.4	0.6	0.8	0.2	0.4	0.6	0.8	0.2	0.4	0.6	0.8
PSNR	Degraded	39.31	36.30	34.51	33.26	33.29	30.28	28.49	27.24	29.76	26.75	24.96	23.72	27.27	24.25	22.47	21.22
	WFAF	52.14	50.32	48.70	47.37	47.32	44.85	43.68	42.75	45.64	41.83	40.24	39.37	42.94	40.22	37.67	36.71
	ASSTV	57.48	54.78	52.96	52.23	53.31	51.85	50.73	49.14	51.17	50.13	48.83	47.83	50.48	48.09	47.09	46.17
	LRMID	59.23	57.67	**56.71**	54.28	54.69	53.59	52.01	51.33	52.73	51.79	49.27	48.88	52.63	49.85	48.21	47.78
	LRMR	47.50	45.53	44.32	43.36	43.91	40.91	39.48	38.29	42.60	40.07	37.52	35.02	41.75	37.51	34.07	33.23
	LRTV	53.93	50.64	46.27	43.18	53.30	49.25	44.22	39.17	53.17	49.12	43.19	38.28	53.20	48.80	43.28	37.24
	LRTFL_0	56.22	54.44	54.10	42.08	56.20	50.83	52.07	38.56	56.90	50.71	45.99	37.09	54.52	**51.66**	46.12	35.14
	NMoG-LRMF	60.27	57.54	48.67	47.00	**60.18**	52.07	44.92	43.55	**57.41**	50.42	41.76	39.95	**55.71**	50.27	39.16	37.53
	AATN	**60.29**	**58.06**	56.42	**56.54**	55.60	**54.43**	**53.41**	**53.21**	54.21	**53.45**	**51.10**	**49.39**	53.30	51.31	**49.28**	**48.72**
SSIM	Degraded	0.8853	0.7856	0.6990	0.6274	0.6835	0.4760	0.3417	0.2526	0.5227	0.2863	0.1634	0.1034	0.4169	0.1817	0.0849	0.0490
	WFAF	0.9904	0.9849	0.9802	0.9717	0.9696	0.9411	0.9323	0.9108	0.9507	0.9006	0.8766	0.8497	0.9214	0.8691	0.8144	0.7719
	ASSTV	0.9974	0.9953	0.9929	0.9916	0.9934	0.9904	0.9882	0.9828	0.9893	0.9854	0.9817	0.9757	0.9863	0.9780	0.9711	0.9627
	LRMID	0.9981	0.9974	0.9969	0.9944	0.9950	0.9933	0.9908	0.9889	0.9922	0.9891	0.9827	0.9795	0.9910	0.9850	0.9756	0.9725
	LRMR	0.9794	0.9683	0.9586	0.9489	0.9543	0.9093	0.8734	0.8287	0.9388	0.8878	0.8262	0.6464	0.9264	0.7988	0.5802	0.5118
	LRTV	0.9956	0.9911	0.9779	0.9481	0.9948	0.9852	0.9617	0.8782	0.9943	0.9789	0.9494	0.8575	0.9939	0.9807	0.9396	0.8094
	LRTFL_0	0.9962	0.9952	0.9951	0.9277	0.9963	0.9876	0.9920	0.8451	0.9967	0.9866	0.9650	0.8080	0.9935	0.9899	0.9642	0.7253
	NMoG-LRMF	0.9985	**0.9979**	0.9852	0.9817	**0.9984**	**0.9942**	0.9662	0.9531	**0.9980**	0.9923	0.9308	0.8984	**0.9970**	**0.9915**	0.8810	0.8290
	AATN	**0.9987**	0.9978	**0.9970**	**0.9966**	0.9957	0.9940	**0.9928**	**0.9927**	0.9933	**0.9924**	**0.9886**	**0.9809**	0.9916	0.9891	**0.9805**	**0.9782**
SAM	Degraded	0.4725	0.6149	0.7074	0.7754	0.7632	0.9300	1.0213	1.0834	0.9469	1.1001	1.1771	1.2277	1.0699	1.2038	1.2660	1.3090
	WFAF	0.1227	0.1470	0.1709	0.1988	0.2121	0.2745	0.3022	0.3382	0.2604	0.3554	0.4011	0.4558	0.3388	0.4266	0.8144	0.5666
	ASSTV	0.0665	0.0910	0.1108	0.1243	0.1042	0.1135	0.1306	0.1664	0.1271	0.1493	0.1602	0.1827	0.1394	0.1813	0.2022	0.2293
	LRMID	0.0563	0.0649	0.0703	0.0994	0.0903	0.0973	0.1156	0.1331	0.1083	0.1266	0.1584	0.1656	0.1114	0.1491	0.1822	0.1969
	LRMR	0.1755	0.2208	0.2552	0.2862	0.2634	0.3811	0.4505	0.5328	0.3046	0.4074	0.5209	0.844	0.3373	0.5712	0.9550	1.0747
	LRTV	0.0568	0.0789	0.1193	0.1980	0.0615	0.1383	0.1804	0.3835	0.0686	0.1847	0.2346	0.4295	0.0757	0.1712	0.2764	0.5307
	LRTFL_0	0.0760	0.0833	0.0788	0.3082	0.0790	0.1364	**0.0888**	0.4232	0.0756	0.1396	0.1858	0.5023	0.1007	0.1156	0.1935	0.6385
	NMoG-LRMF	0.0519	**0.0577**	0.1366	0.1567	**0.0523**	**0.0810**	0.2027	0.2467	**0.0508**	**0.0826**	0.3044	0.3836	**0.0523**	**0.0839**	0.4483	0.5510
	AATN	**0.0476**	0.0625	**0.0696**	**0.0729**	0.0839	0.0935	0.1014	**0.1101**	0.1007	0.1086	**0.1279**	**0.1602**	0.1135	0.1311	**0.1632**	**0.1769**
SID	Degraded	125.96	250.88	378.88	505.41	196.87	393.03	592.06	784.73	310.83	621.43	935.79	1246.54	491.46	991.23	1497.05	1995.22
	WFAF	14.11	21.54	29.26	38.75	39.74	69.53	83.83	99.71	60.12	117.54	144.75	166.37	99.71	146.45	200.73	231.31
	ASSTV	4.16	7.42	11.06	13.01	10.13	14.19	17.42	24.87	15.85	21.23	26.19	33.10	20.13	32.04	40.27	48.17
	LRMID	3.09	4.14	**5.04**	8.59	7.80	10.19	13.44	16.06	11.74	15.55	24.12	27.16	13.46	22.18	32.96	35.12
	LRMR	29.62	46.08	60.78	76.12	66.27	140.14	204.61	281.51	89.71	164.84	242.77	583.04	108.31	318.93	626.11	686.67
	LRTV	5.52	10.60	30.33	74.14	5.96	16.22	51.23	188.59	6.68	18.53	68.43	225.19	6.66	18.45	70.84	259.98
	LRTFL_0	6.24	8.08	7.87	103.82	6.18	19.29	12.97	178.52	5.62	20.33	39.43	241.88	11.15	15.63	40.01	339.13
	NMoG-LRMF	2.85	**3.58**	23.78	30.25	**2.84**	**8.90**	52.41	43.55	**3.33**	11.60	106.28	161.61	**4.77**	**12.72**	194.24	276.03
	AATN	**2.47**	3.74	5.31	**5.57**	6.58	8.98	**10.57**	**11.05**	10.10	**11.22**	**16.34**	**25.03**	12.66	16.75	**26.64**	**28.84**

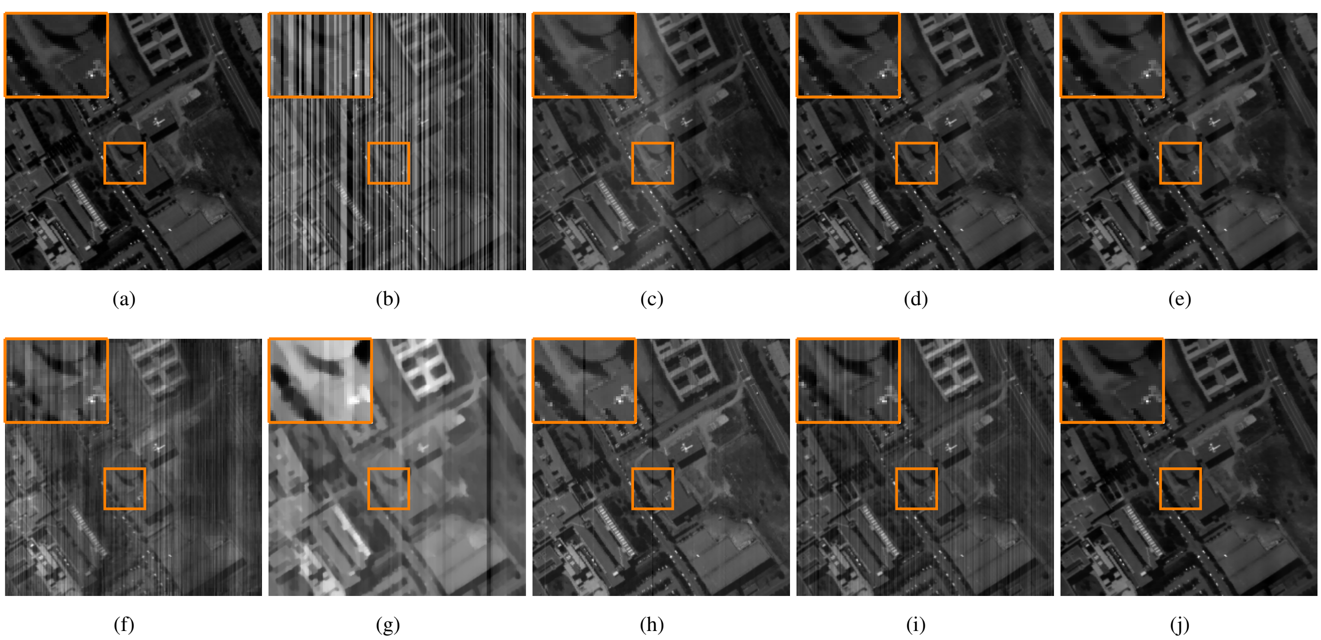

Fig. 9. Band 63 of the University of Pavia image. (a) Original clean image. (b) Striped image ($\eta = 0.4$ and $\gamma = 0.6$). Destriped images generated by (c) WFAF, (d) ASSTV, (e) LRMID, (f) LRMR, (g) LRTV, (h) LRTFL_0, (i) NMoG-LRMF, and (j) AATN.

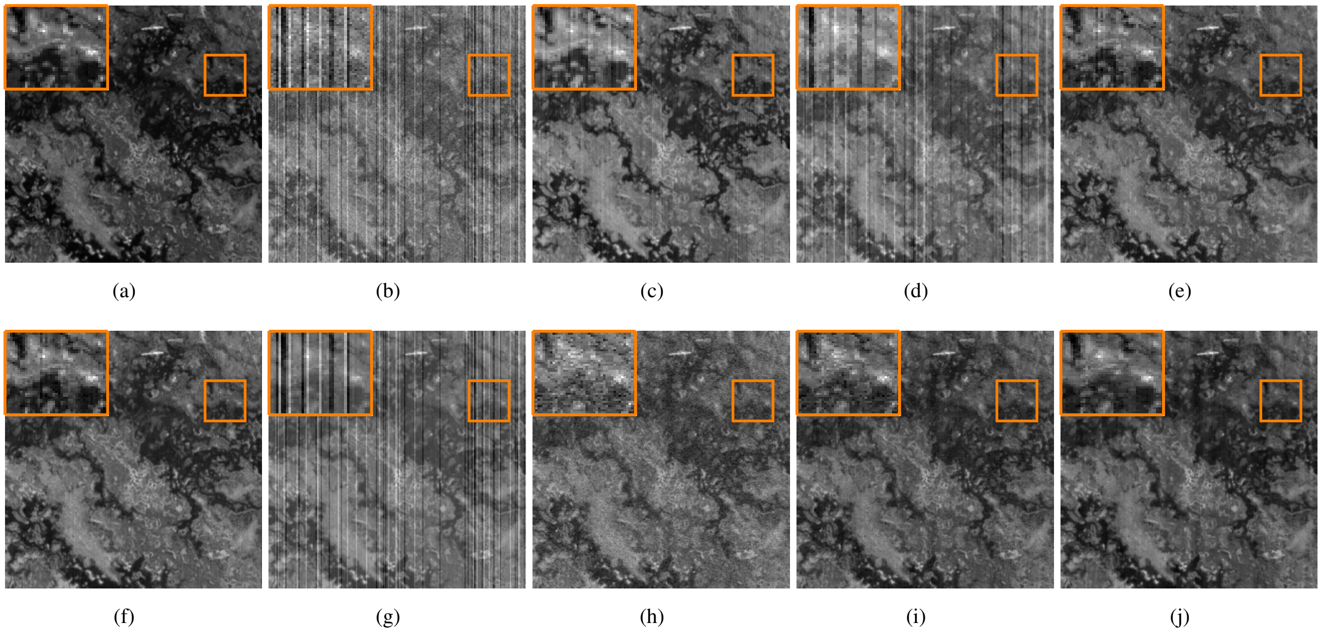

Fig. 10. Band 13 of the Botswana image. (a) Original clean image. (b) Image corrupted with stripes ($\eta = 0.2$ and $\gamma = 0.2$) and Gaussian noise ($\sigma_n = 0.05$). Restored images, generated by (c) LRMR, (d) LRTV, (e) LRTFL_0, (f) NMoG-LRMF, (g) MB-WNN, (h) AATN, (i) W-AATN, and (j) AANNs.

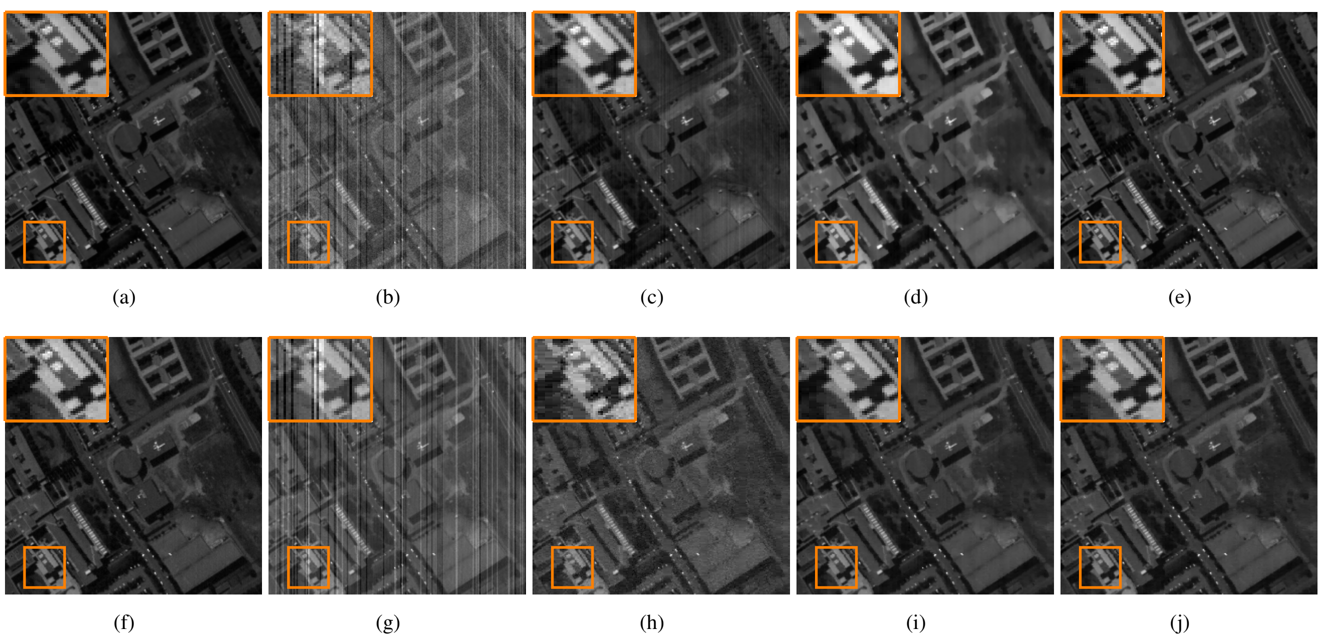

Fig. 11. Band 58 of the University of Pavia image. (a) Original clean image. (b) Image corrupted with stripes ($\eta = 0.2$ and $\gamma = 0.2$) and Gaussian noise ($\sigma_n = 0.05$). Restored images, generated by (c) LRMR, (d) LRTV, (e) LRTFL_0, (f) NMoG-LRMF, (g) MB-WNN, (h) AATN, (i) W-AATN, and (j) AANNs.

TABLE IV
PERFORMANCE METRICS ON THE BOTSWANA IMAGE FOR DIFFERENT LEVELS OF STRIPES AND RANDOM NOISE

Metrics	Method	$\sigma_n = 0.025$		$\sigma_n = 0.05$		$\sigma_n = 0.1$		$\sigma_n \in (0, 0.1]$	
		η, γ		η, γ		η, γ		η, γ	
		0.2, 0.2	0.4, 0.6	0.2, 0.2	0.4, 0.6	0.2, 0.2	0.4, 0.6	0.2, 0.2	0.4, 0.6
PSNR	Degraded	45.89	35.37	45.03	35.29	42.69	34.97	44.87	35.26
	LRMR	54.48	47.26	54.45	46.70	54.16	46.51	54.65	46.54
	LRTV	58.13	51.81	56.31	50.73	54.35	49.36	57.14	51.41
	LRTFL_0	58.48	52.97	56.69	52.73	56.66	50.78	56.45	52.70
	NMoG-LRMF	**62.93**	**53.70**	**61.69**	**53.40**	**59.13**	**53.29**	**62.87**	**53.57**
	MB-WNN	46.39	35.40	46.18	35.40	45.67	35.39	46.20	35.40
	AATN	54.68	52.72	51.30	49.34	46.48	46.80	51.48	50.74
	W-AATN	57.47	52.95	53.38	52.15	51.48	49.33	52.83	51.47
	AANNs	57.14	52.20	55.87	51.55	54.00	50.39	55.40	51.91
SSIM	Degraded	0.9577	0.6871	0.9494	0.6836	0.9183	0.6701	0.9458	0.6821
	LRMR	0.9930	0.9634	0.9925	0.9602	0.9919	0.9591	0.9931	0.9596
	LRTV	0.9916	0.9814	0.9892	0.9766	0.9836	0.9695	0.9906	0.9794
	LRTFL_0	**0.9971**	0.9797	**0.9954**	0.9769	**0.9945**	0.9646	**0.9958**	0.9765
	NMoG-LRMF	0.9414	0.7268	0.9161	0.7055	0.8549	0.6964	0.9399	0.7169
	MB-WNN	0.9625	0.6882	0.9607	0.6882	0.9547	0.6882	0.9606	0.6883
	AATN	0.9934	0.9819	0.9855	0.9789	0.9601	0.9592	0.9818	0.9804
	W-AATN	0.9952	0.9856	0.9916	0.9846	0.9847	0.9732	0.9875	0.9817
	AANNs	0.9954	**0.9873**	0.9944	**0.9860**	0.9912	**0.9811**	0.9934	**0.9850**
SAM	Degraded	0.2396	0.6752	0.2636	0.6796	0.3391	0.6966	0.2743	0.6821
	LRMR	0.0911	0.2097	0.0969	0.2025	0.0939	0.2030	0.0902	0.2033
	LRTV	0.1102	0.1411	0.1249	0.1716	0.1527	0.1936	0.1131	0.2484
	LRTFL_0	0.0555	0.1568	0.0670	0.1687	0.0691	0.2067	0.0646	0.1715
	NMoG-LRMF	**0.0431**	0.1480	**0.0476**	0.1479	**0.0605**	**0.1479**	**0.0445**	0.1535
	MB-WNN	0.2238	0.6739	0.2297	0.6737	0.2479	0.6740	0.2304	0.6736
	AATN	0.0930	**0.1184**	0.1357	0.1468	0.2332	0.2432	0.1587	0.1612
	W-AATN	0.0715	0.1255	0.1000	**0.1314**	0.1411	0.2177	0.1266	0.1462
	AANNs	0.0725	0.1225	0.0819	0.1344	0.0990	0.1508	0.0890	**0.1326**
SID	Degraded	54.02	462.04	65.69	465.64	107.14	477.51	70.06	465.76
	LRMR	13.86	55.30	17.69	66.96	16.12	69.07	14.84	69.47
	LRTV	10.33	35.19	13.68	41.14	21.00	50.75	12.14	36.83
	LRTFL_0	**3.81**	33.62	6.51	34.84	9.41	48.90	13.31	35.35
	NMoG-LRMF	4.04	**28.90**	**4.90**	**28.83**	**6.97**	**29.19**	**4.34**	**28.94**
	MB-WNN	47.69	460.99	50.46	461.11	58.63	461.07	50.37	460.92
	AATN	22.33	32.28	35.55	47.16	66.85	68.96	38.24	41.89
	W-AATN	19.51	35.66	27.00	37.63	33.82	52.53	31.94	40.97
	AANNs	18.69	32.87	20.08	35.14	23.49	37.88	20.71	36.22

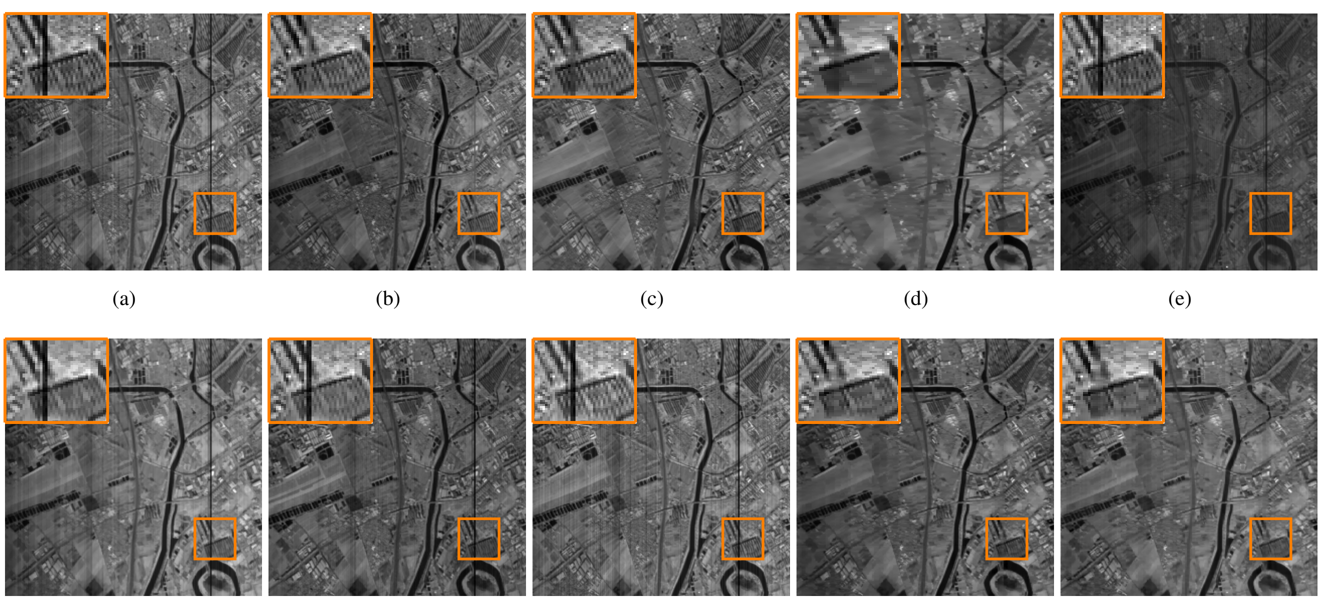

(a) (b) (c) (d) (e)

(f) (g) (h) (i) (j)

Fig. 12. Band 15 of the Tiangong-I image. (a) Original image. Restored images, generated by (b) WFAF, (c) ASSTV, (d) LRMID, (e) LRMR, (f) LRTV, (g) LRTFL_0, (h) NMoG-LRMF, (i) AATN, and (j) AANNs.

TABLE V
PERFORMANCE METRICS ON THE UNIVERSITY OF PAVIA IMAGE FOR DIFFERENT LEVELS OF STRIPES AND RANDOM NOISE

Metrics	Method	$\sigma_n = 0.025$		$\sigma_n = 0.05$		$\sigma_n = 0.1$		$\sigma_n \in (0, 0.1]$	
		η, γ		η, γ		η, γ		η, γ	
		0.2, 0.2	0.4, 0.6	0.2, 0.2	0.4, 0.6	0.2, 0.2	0.4, 0.6	0.2, 0.2	0.4, 0.6
PSNR	Degraded	38.98	28.46	38.12	28.37	35.77	28.06	37.62	28.30
	LRMR	47.57	37.74	47.39	37.90	46.78	37.85	47.21	37.83
	LRTV	51.10	42.68	49.24	41.99	47.23	40.89	49.38	42.84
	LRTFL_0	56.19	47.40	54.44	44.10	49.51	40.82	54.25	43.75
	NMoG-LRMF	**57.87**	44.47	**54.89**	44.48	**50.56**	44.24	**57.45**	44.39
	MB-WNN	39.31	28.49	39.28	28.49	38.38	28.44	39.12	28.48
	AATN	51.27	47.76	46.39	46.74	41.02	42.77	45.31	45.46
	W-AATN	54.59	50.37	52.76	50.14	48.56	**47.67**	52.35	**49.50**
	AANNs	54.51	**50.68**	52.56	**50.18**	49.32	47.52	51.26	49.45
SSIM	Degraded	0.8776	0.3420	0.8551	0.3356	0.7760	0.3189	0.8369	0.3319
	LRMR	0.9796	0.8063	0.9788	0.8124	0.9759	0.8098	0.9780	0.8090
	LRTV	0.9900	0.9376	0.9861	0.9268	0.9781	0.9054	0.9850	0.9437
	LRTFL_0	**0.9968**	0.9794	**0.9948**	0.9540	**0.9877**	0.9069	**0.9956**	0.9499
	NMoG-LRMF	0.9178	0.5507	0.8498	0.5499	0.7356	0.5340	0.9065	0.5448
	MB-WNN	0.8854	0.3415	0.8847	0.3417	0.8625	0.3392	0.8807	0.3414
	AATN	0.9919	0.9808	0.9759	0.9762	0.9226	0.9447	0.9625	0.9670
	W-AATN	0.9959	0.9872	0.9940	0.9867	0.9848	0.9787	0.9933	**0.9857**
	AANNs	0.9959	**0.9886**	0.9927	**0.9872**	0.9865	**0.9790**	0.9905	0.9855
SAM	Degraded	0.4867	1.0227	0.5252	1.0267	0.6388	1.0418	0.5563	1.0302
	LRMR	0.1749	0.4368	0.1773	0.4304	0.1861	0.4340	0.1801	0.4335
	LRTV	0.1194	0.2649	0.1363	0.2916	0.1594	0.3329	0.1380	0.2277
	LRTFL_0	0.0755	0.1460	0.0927	0.2273	0.1337	0.3495	0.0851	0.2398
	NMoG-LRMF	**0.0689**	0.2138	**0.0847**	0.2123	**0.1250**	0.2172	**0.0654**	0.2142
	MB-WNN	0.4727	1.0220	0.4733	1.0222	0.5119	1.0250	0.4806	1.0223
	AATN	0.1352	0.1624	0.2301	0.2029	0.3985	0.3238	0.2845	0.2384
	W-AATN	0.0873	0.1378	0.1089	0.1423	0.1767	0.1944	0.1149	**0.1491**
	AANNs	0.0880	**0.1301**	0.1197	**0.1401**	0.1483	**0.1788**	0.1371	0.1510
SID	Degraded	140.76	597.70	173.50	610.03	264.30	642.05	192.57	617.85
	LRMR	29.39	321.07	30.50	305.97	34.98	309.86	32.00	311.98
	LRTV	13.82	84.76	20.16	100.75	31.65	133.01	21.74	77.32
	LRTFL_0	5.90	31.84	10.07	63.05	22.92	128.33	8.33	68.18
	NMoG-LRMF	**4.61**	58.54	**7.75**	58.22	**17.85**	61.19	**4.48**	59.58
	MB-WNN	128.90	593.87	133.86	595.63	170.65	607.41	139.63	597.03
	AATN	15.49	29.34	42.39	38.36	117.84	86.20	60.41	51.51
	W-AATN	7.55	19.06	11.10	20.01	27.12	33.23	12.25	**21.94**
	AANNs	7.66	**17.33**	12.80	**19.56**	21.65	**31.37**	16.56	22.29

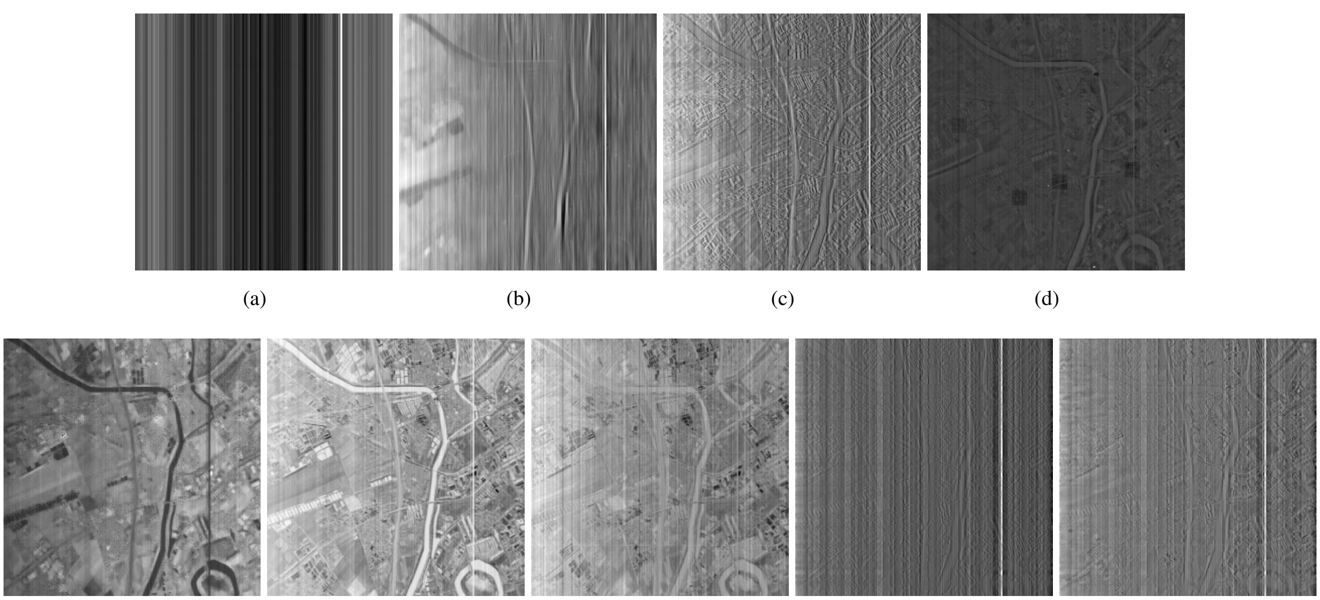

Fig. 13. Residual images of band 15 of the Tiangong-I image, produced by (a) WFAF, (b) ASSTV, (c) LRMID, (d) LRMR, (e) LRTV, (f) LRTFL_0, (g) NMoG-LRMF, (h) AATN, and (i) AANNs.

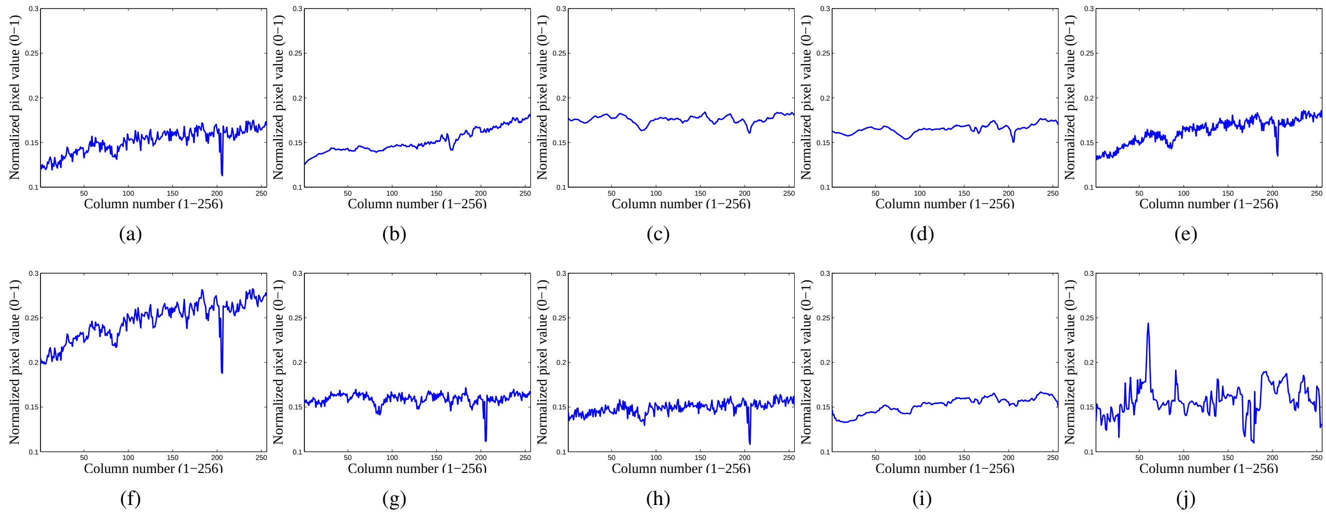

Fig. 14. Mean horizontal profiles of band 15 of the Tiangong-I image. (a) Original image. Restored images, generated by (b) WFAF, (c) ASSTV, (d) LRMID, (e) LRMR, (f) LRTV, (g) LRTFL_0, (h) NMoG-LRMF, (i) AATN, and (j) AANNs. The horizontal axis denotes the image column number (1-256), while the vertical axis represents the normalized pixel value (0-1).

the clean image. From Tables IV-V, it can be observed that AANNs produces stable results, irrespective of the density of stripes, and for both the smooth and the more textured image. Comprehensively, the proposed AANNs outperforms the other image restoration algorithms.

C. Experiments on Real HSI

Due to the lack of the ground truth information, results of the experiments on the Tiangong-I image are visually evaluated. Fig. 12 shows the restored images, Fig. 13 shows the residual images, and Fig. 14 shows the mean horizontal profiles.

Similar conclusions as from the experiments on the synthetic data can be drawn.

- From Figs. 12(b)-12(d) and 14(b)-14(d), it can be concluded that the destriping methods WFAF, ASSTV and LRMID remove most stripes. The enlarged regions, in orange reveal however some remaining stripes. The residual image in Fig. 13(a) is much darker in the middle, revealing a staircase effect caused by WFAF. In the residual images of ASSTV and LRMID (Figs. 13(b) and 13(c)), one can observe quite some image edge information, indicating that these methods oversmooth the image.
- As can be seen from Figs. 12(e)-12(h), LRMR, LRTV, LRTFL_0, and NMoG-LRMF perform poorly on destriping. This can also be observed in the horizontal profiles of their results, which are as rippled as the original profile. Moreover, Figs. 13(d)-13(g) reveal that significant amounts of image information is removed by these methods.
- Although it is hard to find any remaining stripes on the restored image by the proposed restoration method (Fig. 12(j)), the residual image in Fig. 13(i) shows some lost texture information and the profile in Fig. 14(j) appears distorted. One possible cause is the limited amount of Gaussian noise in the Tiangong-I data. The denoising submodel of the proposed method may cause the observed image information loss. The results of the destriping submodel AATN are clearly better. No stripes can be visually observed in Fig. 12(i), hardly any edge information can be found in Fig. 13(h), and Fig. 14(i) shows a smooth horizontal profile with a basic trend that is similar to the original profile.

D. Computational Complexity and Time Performance

The computational complexity of each compared method is summarized in Tabel VI, where the fast addition/subtraction operations are not taken into account. t_1, t_2, and t_3 denote the maximum iterations involved in the compared methods. r' expresses the upper bound of the rank constraint, and r_g is the number of Gaussian models used in NoMG-LRMF. Among the compared destriping methods, the higher the complexity, the better the algorithm performs. For example, the complexity within one iteration is the lowest for the worst performing method WFAF. As for the restoration methods, it is not obvious to discuss their complexities within one iteration because they contain several unknown variables. Here, a rough conclusion can be drawn from the highest order of the complexity. Namely, LRMR and LRTFL_0 are the least and most complex, respectively, while LRTV, NoMG-LRMF, W-AATN and AANNs have similar computational complexity.

To further discuss the complexities of the considered methods, their average execution times, spent on both synthetic and real data are listed in Table VII. All experiments were executed using MATLAB R2014a on a personal computer with Windows 7, with a 64-bit operating system, Intel (R) Core (TM) i7-6700 CPU 3.40 GHz processor, and 16 GB memory. The simulation of our proposed methods was entirely performed with the pseudocode of the corresponding solving procedure; no technique for acceleration was used. The blanks

TABLE VI
COMPUTATIONAL COMPLEXITIES OF DIFFERENT METHODS

Method	Computational complexity
WFAF	$O(t_1 \cdot 4MNB \log_2 MN)$
ASSTV	$O[t_1(6MNB + 4MNB \log_2 MNB)]$
LRMID	$O[t_1(4MNB + 3MNB \log_2 MNB + M^2NB)]$
LRMR	$O[t_1(M-h+1)(N-h+1)(3Bh^2r' + B^2r' + h^2r' + r'^3)]$
LRTV	$O[t_1(M^2N^2B + t_2 \cdot 6MNB)]$
LRTFL_0	$O\{t_1[t_2[(MNB + r'^2)r' \min(M,N) + r'^3 + (M+N)Br'^3[\min(M,N)]^2 + MNr'^2] + t_3MNB]\}$
NoMG-LRMF	$O\{t_1[5MNBr_gr' + 4MNr_gr'^2 + 2(MN+B)r'^3]\}$
MB-WNN	$O\{t_1[4MNB + (M-h+1)(N-h+1)B^2h]\}$
AATN	$O[t_1(4MNB + 3MNB \log_2 MNB + M^2NB)]$
W-AATN	$O\{t_1[4MNB + (M-h+1)(N-h+1)B^2h] + t_2(4MNB + 3MNB \log_2 MNB + M^2NB)\}$
AANNs	$O\{t_1[4MNB + (M-h+1)(N-h+1)B^2h + t_2(4MNB + 3MNB \log_2 MNB + M^2NB)]\}$

in the table denote the unnecessary experiments that were not performed.

Except for the fast WFAF and the slow LRTFL_0, all methods have execution times in the same order of magnitude. The proposed destriping submodel AATN performs on average. Compared to the restoration techniques LRMR, LRTV, LRTFL_0, NMoG-LRMF, and W-AATN, the proposed AANNs is among the fastest. This outstanding time performance can be attributed to the alternating denoising and destriping, that supplement each other in the iteration procedure.

IV. CONCLUSION

In this paper, an HSI restoration method was proposed, that performed denoising and destriping simultaneously. The HSI restoration process was broken down into two, closely related and mutually promoting subtasks: denoising and destriping. Then, the denoising and destriping submodels were proposed. More specifically, the denoising submodel imposed a spectral redundancy constraint on the striped image through a weighted nuclear norm. The destriping submodel contained an adaptive TV regularization that adaptively smoothed the striped image and a truncated nuclear norm regularization to constrain the rank of stripes. Since the striped HSI was the linking bridge between both submodels, a natural combination of both submodels provided the final restoration model. The proposed restoration method was solved under the ADMM framework, alternating denoising and destriping iteratively. Experiments on synthetic and real noisy and striped imagery confirmed the effectiveness and superiority of the proposed restoration approach when compared to the relevant state of the art HSI restoration methods.

REFERENCES

[1] D. Liu, B. Wen, X. Liu, Z. Wang, and T. Huang, "When image denoising meets high-level vision tasks: A deep learning approach," in *International Joint Conferences on Artificial Intelligence Organization*, 2018, pp. 842–848.

[2] M. Zhang, W. Li, and Q. Du, "Diverse region-based cnn for hyperspectral image classification," *IEEE Transactions on Image Processing*, vol. 27, no. 6, pp. 2623–2634, 2018.

[3] U. Muhammad, M. Arif, and M. Ajmal, "Hyperspectral face recognition with spatiospectral information fusion and pls regression," *IEEE Transactions on Image Processing*, vol. 24, no. 3, pp. 1127–37, 2015.

[4] W. Li, G. Wu, and Q. Du, "Transferred deep learning for anomaly detection in hyperspectral imagery," *IEEE Geoscience and Remote Sensing Letters*, vol. 14, no. 5, pp. 597–601, 2017.

[5] N. Liu, W. Li, R. Tao, and J. E. Fowler, "Wavelet-domain low-rank/group-sparse destriping for hyperspectral imagery," *IEEE Transactions on Geoscience and Remote Sensing*, 2019.

[6] W. Zuo, L. Zhang, C. Song, and D. Zhang, "Texture enhanced image denoising via gradient histogram preservation," in *Computer Vision and Pattern Recognition*, 2013, pp. 1023–1210.

[7] A. Barbu, "Training an active random field for real-time image denoising," *IEEE Transactions on Image Processing*, vol. 18, no. 11, pp. 2451–2462, 2009.

[8] K. Zhang, W. Zuo, Y. Chen, D. Meng, and L. Zhang, "Beyond a Gaussian denoiser: Residual learning of deep CNN for image denoising," *IEEE Transactions on Image Processing*, vol. 26, no. 7, pp. 3142–3155, 2016.

[9] Y. Chang, L. Yan, H. Fang, S. Zhong, and W. Liao, "HSI-DeNet: Hyperspectral image restoration via convolutional neural network," *IEEE Transactions on Geoscience and Remote Sensing*, vol. 57, no. 2, pp. 667–682, 2018.

[10] J. Xu, Z. Lei, D. Zhang, and X. Feng, "Multi-channel weighted nuclear norm minimization for real color image denoising," in *IEEE International Conference on Computer Vision*, 2017, pp. 1096–1104.

[11] D. Weisheng, S. Guangming, and L. Xin, "Nonlocal image restoration with bilateral variance estimation: a low-rank approach," *IEEE Transactions on Image Processing*, vol. 22, no. 2, pp. 700–711, 2013.

[12] Q. Yuan, L. Zhang, and H. Shen, "Hyperspectral image denoising employing a spectral-spatial adaptive total variation model," *IEEE Transactions on Geoscience and Remote Sensing*, vol. 50, no. 10, pp. 3660–3677, 2012.

[13] J. Xu, L. Zhang, and D. Zhang, "External prior guided internal prior learning for real noisy image denoising," *IEEE Transactions on Image Processing*, vol. 27, no. 6, pp. 2996–3010, 2018.

[14] L. Sun, R. Neville, K. Staenz, and H. P. White, "Automatic destriping of hyperion imagery based on spectral moment matching," *Canadian Journal of Remote Sensing*, vol. 34, no. sup1, pp. S68–S81, 2008.

[15] P. Rakwatin, W. Takeuchi, and Y. Yasuoka, "Stripe noise reduction in modis data by combining histogram matching with facet filter," *IEEE Transactions on Geoscience and Remote Sensing*, vol. 45, no. 6, pp. 1844–1856, 2007.

[16] H. Carfantan and J. Idier, "Statistical linear destriping of satellite-based pushbroom-type images," *IEEE Transactions on Geoscience and Remote Sensing*, vol. 48, no. 4, pp. 1860–1871, 2010.

[17] J. Chen, Y. Shao, H. Guo, W. Wang, and B. Zhu, "Destriping CMODIS data by power filtering," *IEEE Transactions on Geoscience and Remote Sensing*, vol. 41, no. 9, pp. 2119–2124, 2003.

[18] J. Chen, H. Lin, Y. Shao, and L. Yang, "Oblique striping removal in remote sensing imagery based on wavelet transform," *International Journal of Remote Sensing*, vol. 27, no. 8, pp. 1717–1723, 2006.

[19] R. Pande-Chhetri and A. Abd-Elrahman, "De-striping hyperspectral imagery using wavelet transform and adaptive frequency domain filtering," *ISPRS Journal of Photogrammetry and Remote Sensing*, vol. 66, no. 5, pp. 620–636, 2011.

[20] Y. Chen, T. Z. Huang, and X. L. Zhao, "Destriping of multispectral remote sensing image using low-rank tensor decomposition," *IEEE Journal of Selected Topics in Applied Earth Observations and Remote Sensing*, vol. 11, no. 12, pp. 4950–4967, 2019.

[21] H. Shen and L. Zhang, "A MAP-based algorithm for destriping and inpainting of remotely sensed images," *IEEE Transactions on Geoscience and Remote Sensing*, vol. 47, no. 5, pp. 1492–1502, 2009.

[22] M. Bouali and S. Ladjal, "Toward optimal destriping of modis data using a unidirectional variational model," *IEEE Transactions on Geoscience and Remote Sensing*, vol. 49, no. 8, pp. 2924–2935, 2011.

[23] Y. Chang, L. Yan, H. Fang, and C. Luo, "Anisotropic spectral-spatial total variation model for multispectral remote sensing image destriping," *IEEE Transactions on Image Processing*, vol. 24, no. 6, pp. 1852–1866, 2015.

[24] Y. Chang, L. Yan, T. Wu, and S. Zhong, "Remote sensing image stripe noise removal: From image decomposition perspective," *IEEE Transactions on Geoscience and Remote Sensing*, vol. 54, no. 12, pp. 7018–7031, 2016.

[25] W. Kang, S. Yu, D. Seo, J. Jeong, and J. Paik, "Push-broom-type very high-resolution satellite sensor data correction using combined wavelet-

TABLE VII
AVERAGE EXECUTION TIME (SECONDS) OF DIFFERENT METHODS

Method	Experiments on Synthetic Striped Data		Experiments on Synthetic Striped and Noisy Data		Experiments on Real Data
	Botswana	University of Pavia	Botswana	University of Pavia	Tiangong-I
WFAF	**8.92**	**5.68**	–	–	**2.5**
ASSTV	133.89	98.82	–	–	19.07
LRMID	497.15	384.10	–	–	71.46
LRMR	271.90	220.95	260.96	223.02	58.28
LRTV	270.66	167.78	234.78	179.11	50.69
LRTFL_0	2577.09	1283.85	2162.09	1059.30	1270.98
NMoG-LRMF	181.20	157.26	**200.92**	**181.93**	102.55
MB-WNN	–	–	114.82	90.11	–
AATN	235.93	210.69	240.89	197.09	44.15
W-AATN	–	–	379.08	263.15	–
AANNs	–	–	228.61	195.10	36.24

fourier and multiscale non-local means filtering," *Sensors*, vol. 15, no. 9, pp. 22 826–22 853, 2015.

[26] Y. Chang, L. Yan, H. Fang, and H. Liu, "Simultaneous destriping and denoising for remote sensing images with unidirectional total variation and sparse representation," *IEEE Geoscience and Remote Sensing Letters*, vol. 11, no. 6, pp. 1051–1055, 2014.

[27] H. Zhang, W. He, L. Zhang, H. Shen, and Q. Yuan, "Hyperspectral image restoration using low-rank matrix recovery," *IEEE Transactions on Geoscience and Remote Sensing*, vol. 52, no. 8, pp. 4729–4743, 2014.

[28] W. He, H. Zhang, L. Zhang, and H. Shen, "Total-variation-regularized low-rank matrix factorization for hyperspectral image restoration," *IEEE Transactions on Geoscience and Remote Sensing*, vol. 54, no. 1, pp. 178–188, 2015.

[29] F. Xiong, J. Zhou, and Y. Qian, "Hyperspectral restoration via l_0 gradient regularized low-rank tensor factorization," *IEEE Transactions on Geoscience and Remote Sensing*, vol. 57, no. 12, pp. 10 410–10 425, 2019.

[30] Y. Chen, X. Cao, Q. Zhao, D. Meng, and Z. Xu, "Denoising hyperspectral image with non-i.i.d. noise structure," *IEEE Transactions on Cybernetics*, vol. 48, no. 3, pp. 1054–1066, 2018.

[31] H. Ji, C. Liu, Z. Shen, and Y. Xu, "Robust video denoising using low rank matrix completion," in *Computer Vision and Pattern Recognition*, 2010, pp. 1791–1798.

[32] S. Gu, Z. Lei, W. Zuo, and X. Feng, "Weighted nuclear norm minimization with application to image denoising," in *Computer Vision and Pattern Recognition*, 2014, pp. 2862–2869.

[33] J. F. Cai, E. J. Candes, and Z. Shen, "A singular value thresholding algorithm for matrix completion," *SIAM Journal on Optimization*, vol. 20, no. 4, pp. 1956–1982, 2008.

[34] R. Liu, Z. Lin, F. D. L. Torre, and Z. Su, "Fixed-rank representation for unsupervised visual learning," in *Computer Vision and Pattern Recognition*, April 2012, pp. 598–605.

[35] Z. Wu, Q. Wang, Z. Wu, and Y. Shen, "Total variation-regularized weighted nuclear norm minimization for hyperspectral image mixed denoising," *Journal of Electronic Imaging*, vol. 25, no. 1, p. 013037, 2016.

[36] Z. Wu, Q. Wang, J. Jin, and Y. Shen, "Structure tensor total variation-regularized weighted nuclear norm minimization for hyperspectral image mixed denoising," *Signal Processing*, vol. 131, pp. 202–219, 2017.

[37] B. Du, Z. Huang, N. Wang, Y. Zhang, and X. Jia, "Joint weighted nuclear norm and total variation regularization for hyperspectral image denoising," *International Journal of Remote Sensing*, vol. 39, no. 2, pp. 334–355, 2018.

[38] Y. Hu, D. Zhang, J. Ye, X. Li, and X. He, "Fast and accurate matrix completion via truncated nuclear norm regularization," *IEEE Transactions on Pattern Analysis and Machine Intelligence*, vol. 35, no. 9, pp. 2117–2130, 2013.

[39] J. M. Bioucas-Dias and M. A. T. Figueiredo, "A new twist: two-step iterative shrinkage/thresholding algorithms for image restoration," *IEEE Transactions on Image Processing*, vol. 16, no. 12, pp. 2992–3004, 2007.

[40] D. Yao, L. Zhuang, L. Gao, B. Zhang, and J. M. Bioucas-Dias, "Hyperspectral image inpainting based on low-rank representation: A case study on tiangong-1 data," in *International Geoscience and Remote Sensing Symposium*, July 2017, pp. 3409–3412.

[41] G. Chen, F. Zhu, and P. A. Heng, "An efficient statistical method for image noise level estimation," in *IEEE International Conference on Computer Vision*, 2015, pp. 477–485.

[42] W. Zhou, B. Alan Conrad, S. Hamid Rahim, and E. P. Simoncelli, "Image quality assessment: from error visibility to structural similarity," *IEEE Transactions on Image Processing*, vol. 13, no. 4, pp. 600–612, 2004.

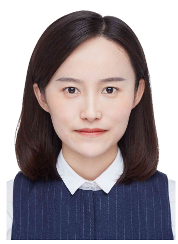

Ting Hu received her B.S. and M.S. degrees from Department of Electronic Information Engineering, Nanchang University, Nanchang, China, in 2014 and 2017.

She is currently pursuing her Ph.D. degree in the School of Information and Electronics, Beijing Institute of Technology, Beijing, China. Her scientific interests include inverse problems for remote sensing image, deep learning, image super-resolution, restoration and denoising.

Wei Li (S'11–M'13–SM'16) received the B.E. degree in telecommunications engineering from Xidian University, Xi'an, China, in 2007, the M.S. degree in information science and technology from Sun Yat-Sen University, Guangzhou, China, in 2009, and the Ph.D. degree in electrical and computer engineering from Mississippi State University, Starkville, MS, USA, in 2012. Subsequently, he spent 1 year as a Postdoctoral Researcher at the University of California, Davis, CA, USA.

He is currently a Professor with the School of Information and Electronics, Beijing Institute of Technology, Beijing, China. His research interests include hyperspectral image analysis, pattern recognition, and data compression. Dr. Li is an associate editor of the IEEE Signal Processing Letters (SPL) and the IEEE Journal of Selected Topics in Applied Earth Observations and Remote Sensing (JSTARS).

Na Liu (S'18) received the B.E. degree from Beijing University of Chemical Technology, Beijing, China, in 2016. She is currently pursuing the Ph.D. degree at Beijing University of Chemical Technology. She is also a visiting Ph.D. student with University of Grenoble Alpes, Grenoble, France, funded by Chinese Scholarship Council. Her research interests include remote sensing data analysis, hyperspectral data enhancement and feature extraction. Her supervisors are Dr. Wei Li and Dr. Jocelyn Chanussot.

Ran Tao (M'00-SM'04) was born in 1964. He received the B.S. degree from the Electronic Engineering Institute of PLA, Hefei, China, in 1985, and the M.S. and Ph.D. degrees from the Harbin Institute of Technology, Harbin, China, in 1990 and 1993, respectively.

In 2001, he was a Senior Visiting Scholar with the University of Michigan, Ann Arbor, MI, USA. He is currently a Professor with the School of Information and Electronics, Beijing Institute of Technology, Beijing, China. He has three books and over 100 peer-reviewed journal articles. His current research interests include fractional Fourier transform and its applications, theory, and technology for radar and communication systems.

Dr. Tao is a member of the Wireless Communication and Signal Processing Commission of International Union of Radio Science (URSI). He was a recipient of the National Science Foundation of China for Distinguished Young Scholars in 2006, and the First Prize of Science and Technology Progress in 2006 and 2007, and the First Prize of Natural Science in 2013, both awarded by the Ministry of Education. He was a Distinguished Professor of the Changjiang Scholars Program in 2009. He was a Chief Professor of the Program for Changjiang Scholars and Innovative Research Team in University from 2010 to 2012. He has been a Chief Professor of the Creative Research Groups of the National Natural Science Foundation of China since 2014. He is currently the Vice Chair of the IEEE China Council and the URSI China Council. He is an associate editor of the IEEE Signal Processing Letters (SPL).

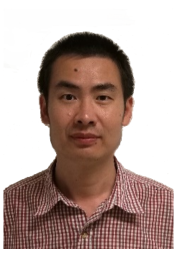

Feng Zhang (M'10) was born in Henan, China, in 1981. He received the B.S. and M.S. degrees from Zhengzhou University, Zhengzhou, China, in 2003 and 2006, respectively, and the Ph.D. degree from the Beijing Institute of Technology, Beijing, China, in 2010. He was a Visiting Scholar with the University of Delaware, Newark, DE, USA, in 2017.

He is currently an Associate Professor with the School of Information and Electronics, Beijing Institute of Technology. His current research interests include time-frequency analysis, fractional Fourier transform, digital image processing, multi sampling rate function processing and machine learning.

Paul Scheunders (Senior Member, IEEE) received the B.S. degree and the Ph.D. degree in physics, with work in the field of statistical mechanics, from the University of Antwerp, Antwerp, Belgium, in 1983 and 1990, respectively.

In 1991, he became a Research Associate with the Imec-VisionLab, Department of Physics, University of Antwerp, where he is a Full Professor. He has published over 200 articles in international journals and proceedings in the field of image processing, pattern recognition, and remote sensing. His current research interests include remote sensing and hyperspectral image processing.

Dr. Scheunders is a Senior Member of the IEEE Geoscience and Remote Sensing Society. He has served as a program committee member in numerous international conferences. He is also an Associate Editor of the IEEE TRANSACTIONS ON GEOSCIENCE AND REMOTE SENSING.